Two-Photon Physics and Online Beam Monitoring Using the DELPHI Detector at LEP

A Thesis Submitted for the Degree of
Doctor of Philosophy in Physics
by

Jonas Bjarne

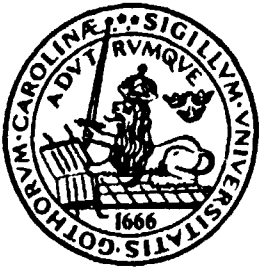

DEPARTMENT OF PHYSICS, UNIVERSITY OF LUND
LUND, 1994

Organization
LUND UNIVERSITY

Department of Physics,
University of Lund, Sölvegatan 14,
S-223 62 Lund, Sweden

Document name
DOCTORAL DISSERTATION

Date of issue September 6, 1994

CODEN: LUNFD6/(NFFL-7089)1994

Author(s)
Jonas Bjarne

Sponsoring organization

Title and subtitle

Two-Photon Physics and Online Beam Monitoring Using the DELPHI Detector at LEP

Abstract

This thesis is based on work done during 1989-1993 using the DELPHI detector at LEP, which is summarised in five articles. It consists of three main parts.

The first part describes the Very Small Angle Tagger (VSAT), which is a sub-detector of the DELPHI detector at LEP. It consists of four silicon-tungsten electromagnetic calorimeter modules having silicon strip planes for position determination. The modules are placed adjacent to the beam pipe, at ± 7.7 m from the interaction point and after superconducting quadrupole magnets, allowing the detection of electrons in a polar angle range of 4 to 13 mrad.

The second part is devoted to two-photon physics at DELPHI, with strong emphasis on a VSAT single-tagged event analysis. Here is shown, for the first time, evidence of hard scattering processes in single tagged two-photon collisions. A QCD Resolved Photon Contribution (QCD-RPC) model is introduced. Data is then seen to be well described by a full VDM+QPM+(QCD-RPC) model. Different parton density functions are compared with data.

The third part first describes the system for online monitoring of LEP beam background and luminosity at the DELPHI interaction point. Details are given of contributing sub-detector signals and program structure. Then follows a description of the VSAT online monitoring program (`VSAT_MONITOR`). A good agreement is found between the `VSAT_MONITOR` estimates of luminosity and beam spot and those of other detectors. Finally, results are presented of VSAT measurements of a LEP beam separation scan.

Key words
LEP, DELPHI, VSAT, electromagnetic calorimeter, two-photon physics, hard scattering, parton density function, online beam monitoring, luminosity, beam spot, beam separati

Classification system and/or index terms (if any)

Supplementary bibliographical information | **Language** English

ISSN and key title | **ISBN** 91-628-1388-

Recipient's notes | **Number of pages** 126 | **Price** | **Security classification**

Distribution by (name and address) Jonas Bjarne, Department of Physics, University of Lund, Sölvegatan 14, S-223 62 Lund, Sweden

ISBN 91-628-1388-9
LUNFD6/(NFFL-7089)1994

Two-Photon Physics and Online Beam Monitoring Using the DELPHI Detector at LEP

By due permission of the faculty of mathematics and natural sciences of the University of Lund to be publicly discussed at the lecture hall F of the Department of Theoretical Physics, September 30, 1994, at 10.15 a.m., for the degree of Doctor of Philosophy

by

Jonas Bjarne
Department of Physics, University of Lund, Sölvegatan 14, S-223 62 Lund, Sweden

This thesis is based on the following articles, included as **Appendices A** to **E**:

A A Silicon-Tungsten Electromagnetic Calorimeter for LEP,
Nucl. Instr. and Meth. A305(1991)320

B Two-Photon Physics at DELPHI,
Proc. of the International Europhysics Conference on High Energy Physics (HEP93)
and DELPHI 93-127 PHYS 342

C First Evidence of Hard Scattering Processes in Single Tagged $\gamma\gamma$ Collisions,
To be submitted to Phys. Lett. B

D The System for Online Monitoring of LEP Beam Background and Luminosity at the DELPHI Interaction Point, DELPHI 93-3 DAS 137

E VSAT Results of the LEP Beam Separation Scan, DELPHI 90-30 GEN 110 MIG 4

Contents

Abstract

This thesis is based on work done during 1989-1993 using the DELPHI detector at LEP, which is summarised in five articles. It consists of three main parts.

The first part describes the Very Small Angle Tagger (VSAT), which is a sub-detector of the DELPHI detector at LEP. It consists of four silicon-tungsten electromagnetic calorimeter modules having silicon strip planes for position determination. The modules are placed adjacent to the beam pipe, at ± 7.7 m from the interaction point and after superconducting quadrupole magnets, allowing the detection of electrons in a polar angle range of 4 to 13 mrad.

The second part is devoted to two-photon physics at DELPHI, with strong emphasis on a VSAT single-tagged event analysis. Here is shown, for the first time, evidence of hard scattering processes in single tagged two-photon collisions. A QCD Resolved Photon Contribution (QCD-RPC) model is introduced. Data is then seen to be well described by a full VDM+QPM+(QCD-RPC) model. Different parton density functions are compared with data.

The third part first describes the system for online monitoring of LEP beam background and luminosity at the DELPHI interaction point. Details are given of contributing sub-detector signals and program structure. Then follows a description of the VSAT online monitoring program (`VSAT_MONITOR`). A good agreement is found between the `VSAT_MONITOR` estimates of luminosity and beam spot and those of other detectors. Finally, results are presented of VSAT measurements of a LEP beam separation scan.

Preface

This thesis, submitted for the degree of Doctor of Philosophy in Physics, gives a survey of the work I've done for the DELPHI Collaboration as a postgraduate student. Not included are all the dead-ends and mistakes experienced by most students, like me!

The resulting five physics articles are included at the end of the thesis, as Appendix A to Appendix E. They are preceeded by an introductory text containing relevant theory and terminology, as well as extensions and summaries of the papers. The VSAT online monitoring program, not included in any article, is also described.

My first encounter with elementary particle physics was during the summer of 1988, when I, as a CERN Summer Student, worked together with people of the LEP Beam Instrumentation group. My contribution, later resulting in a B.Sc. thesis [1], consisted of participating in program development for and beam tests of the LEP luminosity monitors [2]. I also participated in initial prototype tests of the DELPHI VSAT, modelled after the LEP luminosity monitors, using the same test set-up.

Staying at CERN from early 1989 to late 1991, most of my time was spent setting up and working with the VSAT detector (Appendix A). I concentrated on working with online monitoring in DELPHI (Appendix D) and, in particular, the extraction of monitoring information from the VSAT (Appendix E). My main responsability was writing the VSAT online monitoring program.

Later, staying in Lund, an exciting time was spent working with two Russian visiting scientists and friends, analysing DELPHI two-photon data. With VSAT-tagged data, the first evidence was found for hard scattering processes in single-tagged two-photon collisions (Appendix C). This, together with other DELPHI two-photon results, were reported by me at the HEP 93 conference in Marseille (Appendix B).

Summing up my views of these years, I'd like to quote an Italian Summer Student working for the VSAT group a few years ago:

> *I think I have been very lucky to work inside the VSAT group that maintains a peculiar dimension in search of a singular reality.*

After this, what can I add? I have enjoyed it!!!

Jonas Bjarne
Lund, August 1994

Chapter 1

Apparatus

Below is given a short overview over the apparatus used for this work. LEP and DELPHI are first briefly described, followed by a more detailed description of the VSAT sub-detector.

1.1 The LEP Collider

The **Large Electron-Positron collider (LEP)** is the largest collider ever built. It was designed by engineers and physicists from CERN and built by the European industry. The, at that time, 14 CERN member states contributed the 1300 million Swiss francs required for its construction. Planning started in September 1978, the first electron-positron collisions were produced on August 13, 1989, while the machine was officially inaugurated on November 13, 1989. The LEP collider has been described by several other authors, ranging from popular to more technical papers [3]-[5]. Below will be given only a very short summary of some key LEP parameters.

The LEP tunnel is placed outside of Geneva, on the borderland between Switzerland and France. It is roughly circular with a circumference of almost 27 km. The construction consists of eight straight 500 m sections connected by eight 2800 m arcs. Underground depth varies between 50 and 175 m. The tunnel inside diameter is 3.8 m, except for the four large experimental halls having diameters 23 m and lengths 80 m.

The LEP particle injection scheme is rather complex, using four smaller accelerators and storage rings before injection into LEP. The electrons and positrons are divided into four (later changed to eight) bunches each. Each bunch contains about 10^{11} particles, corresponding to a current of 3 mA per circulating beam. At the interaction points the bunches have strongly elliptical cross-sectional areas of around 210 μm (horisontally) times 8 μm (vertically). Longitudinal length is around 1.1 cm. Maximum LEP luminosity is 1.7×10^{31} cm^{-2}s^{-1}, but normal luminosities seldom exceeded 1×10^{31} cm^{-2}s^{-1} during the 1989-1992 runs.

Particle injection energy is 20 GeV, with further acceleration being performed by LEP. Standard final beam energy is 45.625 GeV, this being optimal for studying the Z^0 resonance at 91.25 GeV. In 1996 LEP will be upgraded to a new phase, called LEP200. Beam energy will then be around 90 GeV to allow detailed studies of the W resonance.

1.2 The DELPHI Detector

One of the four detectors at LEP is **DELPHI, a DEtector with Lepton, Photon and Hadron Identification**. Though DELPHI is a general purpose detector special emphasis is put on powerful particle identification, three-dimensional information with high granularity and precise vertex determination.

The DELPHI detector is shaped like a cylinder with the beam pipe along the cylinder axis (Figure 1.1). It has a radius of 5 m and a length of 10 m. DELPHI is divided into a cylindrical barrel part and two conical end-cap parts. The transition regions, at polar angles 43° and 137°, are partially obscured by cables and connectors. The end-caps can be pulled out from the barrel. A superconducting solenoid is installed at a radius of 2.6 m, providing a uniform magnetic field of 1.2 T along the beam-pipe when an electric current of 5000 A floats through it. DELPHI is installed in a cavern 100 m below ground. Data is sent *via* an optical link to the main computer and control room at ground level.

DELPHI is a complex detector system consisting of around 20 sub-detectors. A brief description will be given below only of those of main interest to this work, *i.e.* charged particle tracking devices and electromagnetic calorimeters. The VSAT is treated in more detail. More information about the DELPHI detector can be found in [6]. Though DELPHI has evolved over the years, with many performance upgrades, the description below is based mainly on this report.

The coordinate system is defined to have the z-axis along the beam pipe. Polar angles θ are given with respect to z, while azimuthal angles ϕ are given starting from the horizontal plane. Radii is denoted by R.

1.2.1 Charged Particle Tracking Devices

The **micro-VerTeX (VTX)** consisted initially of two concentric silicon-strip shells surrounding the beam pipe. They have radii 9 and 11 cm and lengths 24 cm, covering a θ-range of 37° to 143°. Each shell is built of 24 ϕ modules, each module having four z segments. A third silicon-strip shell was later added when the beam-pipe at the DELPHI interaction point was changed to a tube of smaller diameter. Three $R\phi$-points per track are now measured. The intrinsic $R\phi$ resolution is 6 μm.

The **Inner Detector (ID)** [7] consists of two concentric parts. The inner part is a jet chamber having an inner radius of 12 cm, an outer radius of 22 cm and a z-length of 80 cm. This results in a θ-coverage of 17° to 163°. The jet chamber provides 24 $R\phi$-points per track through its 24 ϕ sectors, each having 24 sense wires. A coordinate resolution of 90 μm in the $R\phi$-plane is obtained. The outer part of the ID is a multi-wire proportional chamber (MWPC). Its radial placement is between 23 and 28 cm, length is 50 cm along z and θ-coverage is from 30° to 150°. The MWPC contains five concentric layers, each having 192 wires and circular cathode strips. The wires provide fast trigger information (>95% single track trigger efficiency) while the strips measure z with a resolution of <1 mm.

The main tracking device is a **Time Projection Chamber (TPC)** [8]. It consists of two cylindrical parts placed after each other along the beam pipe. Each part has an active z-length of 134 cm, with inner and outer radii of 35 and 111 cm respectively. θ is measured between 20° and 160°. The two cylindrical parts are

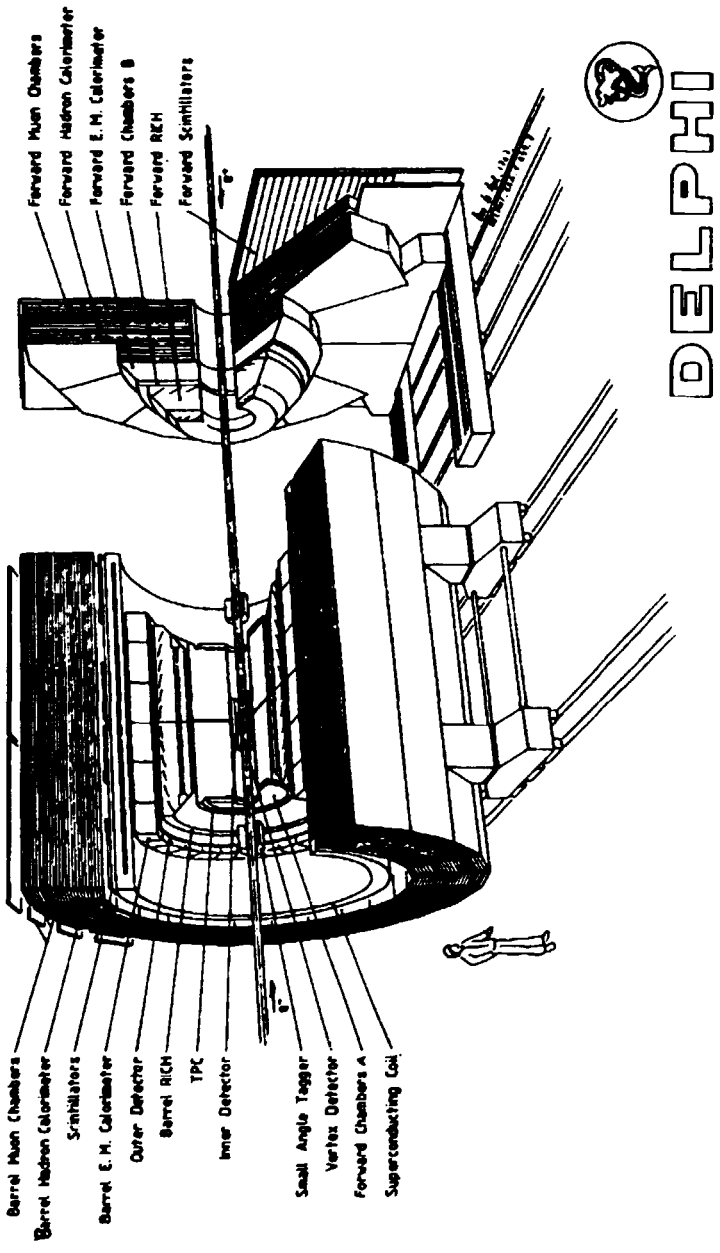

Figure 1.1: The DELPHI detector. The VSAT modules, at $|z| = \pm 7.7$ m, fall outside this figure.

each divided into six sectors in ϕ, each such sector having 16 radial pad rows and 192 sense wires. The pads give 16 points per track in the $R\phi$-plane, resulting in a resolution of 230 μm. A z-resolution of 900 μm is reached through the 192 track points provided by the wires.

The outermost tracking device is the **Outer Detector (OD)** [9], composed of 24 modules in ϕ. Each module is 4.7 m along z, has an inner radius of 198 cm and an outer radius of 206 cm. This leads to a θ-coverage between 43° and 137°. There are five radial layers of drift tubes per module. All the layers measure the $R\phi$-coordinate with a resolution of 110 μm. Three of them also contribute to a z-measurement with a resolution of 4.4 cm.

Each end-cap contains two **Forward Chambers (FCA, FCB)** for tracking in the forward and backward regions (θ from 11° to 35° and 145° to 169° respectively). FCA is the inner one, having R and $|z|$ extensions of 30 to 103 cm and 155 to 165 cm. Each FCA-side contains three double layer half-disc chambers, rotated 120° in ϕ with respect to each other. The layers consist of square cells (15 mm side) with an anode wire in the centre. Six track points are measured by FCA with a total resolution of 150 μm in the $R\phi$-plane. FCB covers R between 53 and 195 cm and $|z|$ between 267 and 283 cm. It also consists of double layer half-disc chambers, but each half-disc is for the FCB divided into six ϕ segments. Each segment consists of 12 pair-wise rotated sense wire planes, having a wire spacing of 2 cm. The 12 track points result in an FCB $R\phi$-resolution of 120 μm.

1.2.2 Electromagnetic Calorimeters

The **Forward ElectroMagnetic Calorimeter (FEMC)** [10]-[12] consists of two modules, one on each end-cap, situated between $|z|$-values of 284 and 340 cm. Each module is in the form of a disk having radial extension from 46 to 240 cm. The θ-acceptance is from 10° to 36.5° for the forward module, and from 143.5° to 170° for the one in the backward direction. A module is built of 4532 lead glass blocks in the form of truncated pyramids. They are arranged to point towards the interaction point. Each pyramid is 20 radiation lengths deep and has a granularity of one degree in both θ and ϕ. Read-out is *via* vacuum phototriodes. FEMC has a 4% energy resolution at a beam energy of 45.6 GeV.

The **Small Angle Tagger (SAT)** [13] also consists of two end-cap modules. They are placed longitudinally between $|z|$ 233 and 285 *cm*, and radially between 10 and 36 *cm*. The SAT modules cover a θ-range of 2.5° to 7.7° (172.3° to 17.5°) in the forward (backward) direction. Each calorimeter module is built from alternating lead sheets and plastic scintillating fibres, which are aligned parallel to the beam-pipe. Read-out is *via* lightguides and photodiodes, segmented in the $R\phi$-plane to have a granularity in ϕ of 7.5° (15°) for the inner (outer) four radial rings, while θ-granularity is 0.7°. The 28 radiation lengths deep modules have energy resolutions of 1.6% at a beam energy of 45.6 GeV. For the 1994 runs the SAT was replaced by a **Small angle TIle Calorimeter (STIC)** [14, 15].

1.2.2.1 The VSAT Sub-Detector

The **Very Small Angle Tagger (VSAT)** is described in detail in Appendix A.

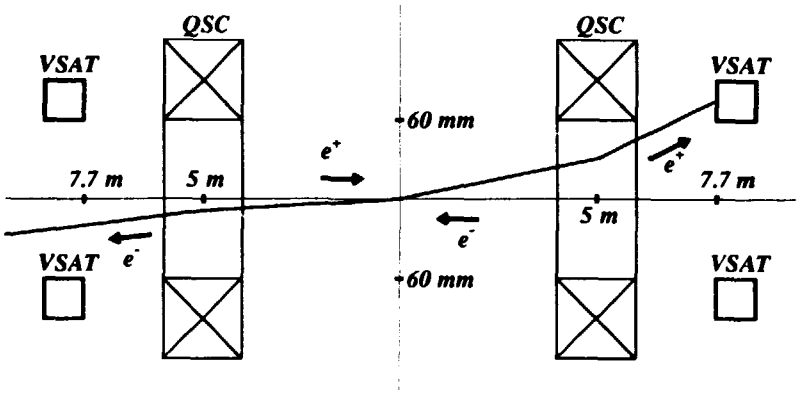

Figure 1.2: Picture (not to scale) of the LEP beam transport around the DELPHI interaction point. The four VSAT modules are placed symmetrically at ± 7.7 m from the interaction point, and on both the inner and outer sides of the LEP ring. The trajectories of charged particles are bent in the superconducting quadrupole magnets (QSC) in front of the VSAT modules.

Here only a summary will be given of some main VSAT features, together with a few extensions and figures to complement the reading of Appendix A.

The VSAT consists of four electromagnetic calorimeter modules placed at ± 7.7 m from the interaction point, *i.e.* after the superconducting quadrupole magnets (QSC) as shown in Figure 1.2. The modules are placed horisontally around short elliptical sections of the beam pipe, with one module on each side of it (left picture in Figure 1.3).

The QSC's in front of the VSAT modules, focusing outgoing charged particles in the vertical direction and defocusing them in the horisontal direction, distorts the VSAT (θ,ϕ)-acceptance. The VSAT acceptance above 20 GeV has a usable θ-range from 4 to 13 mrad. The ϕ-coverage, while about $\pm 45^\circ$ around the horisontal axis per module at nominal beam energy, increases for lower energies due the QSC focusing.

Each VSAT calorimeter module contains 12 two radiation lengths thick tungsten absorbers, stacked with 12 silicon detector planes for energy measurements (right picture in Figure 1.3). The overall active size for each calorimeter stack is 3 cm horisontally and 5 cm vertically with a depth of 10 cm (24 radiation lengths). However, due to the beam pipe flanges in front of the VSAT modules, the area illuminated by particles is only 1.5 cm horisontally. The resulting energy resolution for transversely contained showers is $35\%/\sqrt{E}$, *i.e.* $\sim$5% at nominal beam energy.

Horisontal and vertical electromagnetic shower coordinates are measured by three silicon strip planes (1 mm pitch) placed at 5, 7 and 9 radiation lengths into each stack, this being close to the shower maxima. Two strip planes measure x-coordinates and one y-coordinate. Strip information is used to eliminate showers being too close to a calorimeter edge, as well as to correct for transversal shower

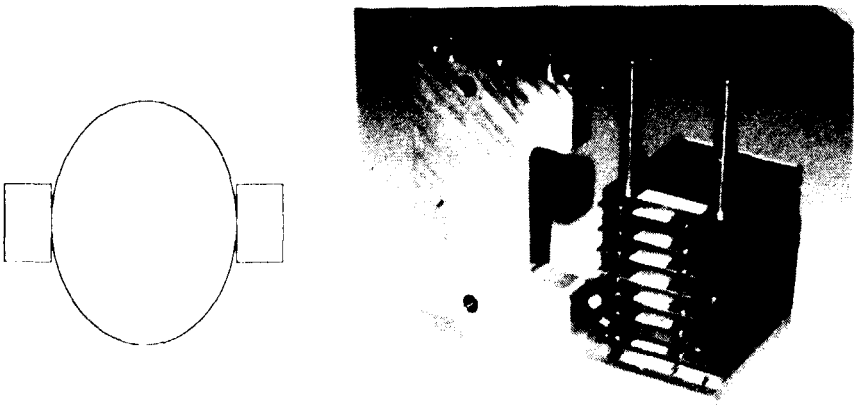

Figure 1.3: Transversal view of the beam pipe, showing the placement of two VSAT modules around an elliptical beam pipe section (left picture). Photo of a dismounted VSAT calorimeter module, showing the stacking of silicon detector planes and tungsten energy absorbers (right picture).

leakage. The reconstructed position resolution is about 200 μm.

The VSAT provides three kinds of triggers:

- A Bhabha event is defined as the coincidence between diagonal modules, each module detecting at least an energy of 20 GeV.
- Bremsstrahlung off-momentum beam particles, called Single Electrons, are recorded by a downscaled trigger also having a 20 GeV threshold.
- Accidental diagonal coincidences, called False Bhabhas, are recorded by a trigger requiring a Single Electron in an inner module and another one in its diagonal (outside) module N bunches later (N = the number of LEP bunches).

Any VSAT event is accompanied by trigger information to DELPHI . This information can be used by other DELPHI subtriggers for trigger decisions.

Since the VSAT trigger rate is higher than the DELPHI trigger rate, VSAT events are accumulated in a local event buffer which is read out at each DELPHI event. A DELPHI event is forced by VSAT when the event buffer is full, which rarely happens.

Chapter 2

Two-Photon Physics

Classical electromagnetic theory only allows the superposition of two crossing electromagnetic waves, but no interaction between them. Photon-photon interactions are instead allowed by modern quantum electrodynamic theory (QED). However, the probability for these interactions is extremely small at low energies, preventing two-photon interactions to be observed with even the strongest of photon beams, like lasers. These interactions have instead been studied using colliding electron and positron beams. By QED radiative quantum effects the electrons and positrons are surrounded by clouds of virtual photons. The circulating e^+e^- beams of a collider can thus be seen to be the sources of two strong photon beams.

These photon beams have some special properties. The resulting photon luminosities are normally quite high, only about a magnitude smaller than the e^+e^- luminosities. As the cross-section for two-photon scattering increases with beam energy E ($\sim \log^2(E/m_e)$), high-energy colliders are ideal machines for two-photon studies. The photons are radiated according to a Bremsstrahlung-like spectrum (probability $\sim 1/E_\gamma$), and mainly into small angles ($\sim m_e/E$) relative to the beams. This leads to a dominance of two-photon events having low invariant masses W. Since normally the two radiated photons have different energies, most two-photon event axes are strongly boosted along the e^+e^- beam direction. Here particles are more difficult to detect, making the visible (*i.e.* detected) cross-section appreciably smaller than the true (*i.e.* total) cross-section. Note that the energy spectra of the photons allow different values of W to be measured, while the e^+e^- kinematics which is fixed by the e^+e^- beam energy.

Two-photon studies have been performed by many e^+e^- experiments, *e.g.* at DESY by PLUTO [16], at SLAC by TPC/2γ [17] and at KEK by AMY [18]. Recently, two-photon results have also been presented by all the four LEP experiments (ALEPH [19], DELPHI, L3 [20] and OPAL [21]).

The two-photon results obtained with the DELPHI detector are described below, with emphasis on the analysis of VSAT-tagged events. This is preceeded by a short introductory theoretical background to the field of two-photon physics.

2.1 Theoretical Background

Below is given a very brief introduction to two-photon theory, discussing competing processes before concentrating on two-photon kinematics, tagging and models.

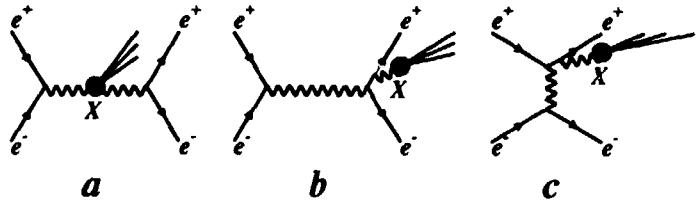

Figure 2.1: Feynman diagrams of (a) the γ cascade process, (b) the virtual Bremsstrahlung process with e^+e^- annihilation and (c) the virtual Bremsstrahlung process with e^+e^- scattering.

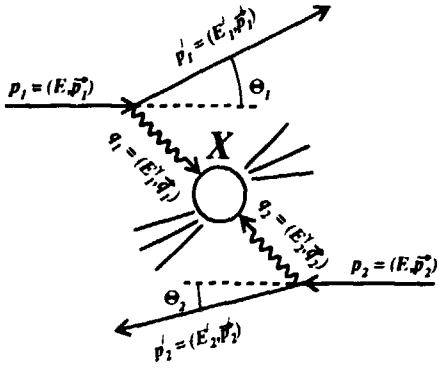

Figure 2.2: Kinematics of the two-photon process.

More detailed descriptions can be found in Appendix C as well as in several other papers [22]-[27].

2.1.1 Processes

Inelastic electron-positron processes ($e^+e^- \rightarrow e^+e^- + X$, where X is a particle system) can be classified as

- γ cascade processes
- virtual Bremsstrahlung processes with e^+e^- annihilation
- virtual Bremsstrahlung processes with e^+e^- scattering
- two-photon processes

Feynman diagrams over these processes are shown in Figure 2.1 and Figure 2.2. In each of these diagrams a photon propagator can be replaced by a Z^0 particle. However, due to the very high mass of the Z^0 boson ($m_{Z^0} \approx 91$ GeV), the diagrams

with Z^0 propagators are heavily suppressed and will not be considered further in this thesis.

The amplitudes of the diagrams depend on the propagation factors $1/q_i^2$, where q_i is the momentum transfer of propagator i. The diagrams of Figs. 2.1.1a and 2.1.1b are one-propagator e^+e^- annihilation diagrams, with $q = \sqrt{s} = 2E_{beam}$ for a collider. At the high beam energies of LEP ($E_{beam} \approx 46$ GeV) the amplitudes of these diagrams are negligible. The one-propagator diagram of Fig. 2.1.1c has the propagation factor $1/q^2$, while the two-propagator diagram of Fig. 2.1.1 has a total factor of $1/q_1^2 \cdot 1/q_2^2$. In this thesis will be considered the case with very small momentum transfers q, leading to a dominance of the latter diagram. It is thus seen that the two-photon diagram of Fig. 2.1.1 is the dominant diagram at the beam energies and momentum transfers of concern for this work.

2.1.2 Kinematics

The momentum transfer Q_i^2 in each lepton-photon vertex i in the two-photon reaction can be calculated as (see Fig. 2.1.1)

$$-Q_i^2 = q_i^2 = (p_i - p_i')^2 = 2m_e^2 - 2EE_i'(1 - \sqrt{1-(m_e/E)^2} \cdot \sqrt{1-(m_e/E_i')^2} \cdot \cos\vartheta_i), \tag{2.1}$$

which, for $\theta_i \gg m_e/E$, can be approximated by

$$-Q_i^2 = q_i^2 \approx -4EE_i' \sin^2(\theta_i/2) \tag{2.2}$$

At LEP $m_e/E \approx 10^{-5}$. This is indeed much smaller than the polar angles θ_i in which it is possible to detect the scattered leptons at DELPHI, meaning that (2.2) is applicable.

With $E_i^\gamma = E - E_i'$ the invariant mass W of the produced particle system X is given by

$$W^2 = (q_1 + q_2)^2 = 4E_1^\gamma E_2^\gamma - 2E_1'E_2'(1 - \cos\theta_1\cos\theta_2 - \sin\theta_1\sin\theta_2\cos\Phi) \tag{2.3}$$

Here Φ is the angle between the two planes defined by the two scattered leptons and the beam axis. Since we will here only treat the case with very low momentum transfer scattering, equation (2.3) can be simplified to

$$W^2 \approx 4E_1^\gamma E_2^\gamma \tag{2.4}$$

2.1.3 Tagging

Experimentally one can detect the energy and angles of both, one or none of the leptons scattered from the two-photon reaction. This is called "tagging" the interacting photons. One differentiates between the four cases of double-tagging, single-tagging, no-tagging and anti-tagging. Tagging is normally done by detectors placed in the forward regions, typically covering $\theta < 100$ mrad.

2.1.3.1 Double-tagging

In this case, knowing both photon four-vectors, the full reaction kinematics is available for precise cross-section studies *etc.* Double-tagging also ensures a complete dominance of the two-photon diagram over competing diagrams. However, experimental limits on the W resolution severely limit the obtainable accuracy. An unfolding procedure is often required to link the visible W to the true W. Due to the strong forward peaking of the scattered leptons, tagging needs to be done at very small angles. Here high-rate background sources, such as small angle Bhabha scattering, can be difficult to reject. The experimentally visible cross-section for double-tagged two-photon events is very small.

2.1.3.2 Single-tagging

Detecting either the scattered electron or the positron is necessary for studying the Q^2 dependence of, for example, the photon structure function F_2^γ. The Q^2 of the virtual photon, which probes the target photon structure, is given by the measurement of the tagged lepton. Large Q^2-values are required to enter into the deep inelastic scattering range, implying rather large scattering angles ($\theta_{tag} > 100$ mrad). Here the cross-section is comparatively small due to the forward peaking of the leptons. Moving to the low-Q^2 range ($\theta_{tag} < 30$ mrad) the event rate goes up, and one can, by analysing relatively high-$W_{\gamma\gamma}$ events, study the production and properties of jets with high transverse momenta p_T. The measured energy spectrum of the leptons can be useful in this analysis. Resonance formation studies can also be carried out with single-tagged two-photon events. Detecting a scattered lepton is useful for reducing different background sources, like e^+e^- annihilation processes. One has to make sure that the non-detected electron is not scattered into large angles (*i.e.* large Q^2), as the virtual Bremsstrahlung process with e^+e^- scattering (Fig. 3.1c) will then dominate. Experimentally visible cross-sections for single-tagged two-photon events, though dependent on Q^2, are typically at least 10 times larger than for the double-tagged case.

2.1.3.3 No-tagging

Not detecting any of the scattered leptons, the only information available is that of the produced particle system X. However, two-photon reactions generally involve small momentum transfers Q^2, implying also comparatively low W. Also the no-tagged events can be used for studying low-p_T jets, resonances *etc.* The two-photon process is dominant at low W, reducing the background contamination from other processes such as the one-photon reaction $e^+e^- \rightarrow X$. It is also necessary to require low-Q^2 scattering in order to ensure this dominance; only accepting events with small total p_T ensures a sample being completely reconstructed. Not requiring any tagging greatly increases the visible cross-section, this being at least a factor 100 larger than for the double-tagged case.

2.1.3.4 Anti-tagging

It is shown above that in order to ensure the dominance of the two-photon

process, it is necessary for the single-tagged and no-tagged cases to require the untagged leptons to have small scattering angles. This can be done by an anti-tagging requirement, where an event is rejected if two leptons (one for the no-tagged case) are detected. Having a detector in the very forward direction thus assures very low Q^2 for the untagged leptons.

2.1.4 Cross-Sections

Two-photon cross-section calculations are in general quite lengthy and complicated. Using some approximations, the cross-section $\sigma_{\mu\mu}$ for $e^+e^- \rightarrow e^+e^-\mu^+\mu^-$ is, however, seen to be a managable and instructive case [28]. The QPM model, discussed later, is based on calculations analogous to what will be described below. The $\mu^+\mu^-$ production is given by the QPM-diagram of Figure 2.3.b, where $q\bar{q}$ should be replaced by $\mu^+\mu^-$. This diagram can be divided into two parts, the first one describing $e^+e^- \rightarrow \gamma\gamma$ and the second $\gamma\gamma \rightarrow X \rightarrow \mu^+\mu^-$. Only the no-tag case is treated here.

The Bremsstrahlung spectrum of the beam-radiated photons can be approximated by the Weizsäcker-Williams formula, with $\omega = E^\gamma/E$ and $\alpha \approx 1/137$

$$\frac{dN}{d\omega} = \frac{\alpha}{2\pi}\frac{1+(1-\omega)^2}{\omega}\ln\left(\frac{E^2}{m_e^2}\right) \tag{2.5}$$

The convoluted photon spectra at some W define a two-photon luminosity function $L_{\gamma\gamma}$. Its dependence on the energy fraction $\tilde{s} = W/\sqrt{s} = W/2E$ is given by

$$\frac{dL_{\gamma\gamma}}{d\tilde{s}} = \left(\frac{\alpha}{\pi}\right)^2 \frac{f(\tilde{s})}{\tilde{s}} \ln^2\left(\frac{E^2}{m_e^2}\right) \tag{2.6}$$

with

$$f(\tilde{s}) = (2+\tilde{s}^2)^2 \ln\left(\frac{1}{\tilde{s}}\right) - (1-\tilde{s}^2)(3+\tilde{s}^2) \tag{2.7}$$

This approximation describes the shape of $L_{\gamma\gamma}$ well, but overestimates its value by around 10% for $\tilde{s} < 0.8$.

By finally convoluting $L_{\gamma\gamma}$ with the approximated cross-section $\sigma_{\gamma\gamma} = 4\pi\alpha^2/W^2$ for $\gamma\gamma \rightarrow X \rightarrow \mu^+\mu^-$, the total cross-section $\sigma_{\mu\mu}$ becomes

$$\sigma_{\mu\mu} = \int L_{\gamma\gamma}\,\sigma_{\gamma\gamma}\,d\tilde{s} = \frac{8\alpha^4}{\pi}\frac{1}{m_\mu^2}\ln^2\left(\frac{E}{m_e}\right)\ln\left(\frac{E}{m_\mu}\right) \tag{2.8}$$

Notice the $\ln E$ dependence of $\sigma_{\mu\mu}$, showing the increasing two-photon cross-section with energy.

2.1.5 Models

The photon is a complex object to describe, as it shows several different characteristics. Results from some experiments (photoproduction, electromagnetic form factors *etc.*) show the characteristics of soft hadron interactions. Other experiments (*e.g.* high energy e^+e^- annihilation) show a direct coupling to pointlike quarks inside the hadrons. The first characteristic is described by the VDM model, while the

second is described by the QPM model. Until recently, a composite VDM+QPM model was able to explain all two-photon data. However, several experiments ([29]-[31]) have reported high-p_T event excesses which can not be explained inside this model. A third component, the QCD-based hard scattering model, has therefore been added to better describe the data. The latter model requires specific parton density functions to calculate parton momenta fractions. Below is given a very brief overview over these models.

2.1.5.1 The VDM Model

The non-perturbative, phenomenological **Vector meson Dominance Model (VDM)** (Figure 2.3.a) is well-known from hadron-hadron interaction physics. To describe the interaction between a photon and hadrons, VDM assumes the photon to convert into vector mesons. These then interact with hadrons through the strong force. VDM thus predicts photon-photon scattering to have the characteristics observed for hadron-hadron scattering. VDM is only applicable for small transverse momenta p_T, where the lifetime of the quark-antiquark pair is long enough for them to interact *via* gluon exchange to form bound vector meson states. The main contribution to the total two-photon cross-section comes from VDM processes.

The VDM cross-section is given by [32] as

$$\sigma_{\gamma\gamma}^{VDM}(Q_1^2, Q_2^2, W^2) = F_{VDM}(Q_1^2) F_{VDM}(Q_2^2) \left[A + \frac{B}{W} \right] \tag{2.9}$$

The last term, in brackets, describes the W-dependence of $\sigma_{\gamma\gamma}$. The underlying theory here is the Regge model, resulting in a W-behaviour of $W^{2\alpha-2}$ [33]. Treating only the terms with α=1/2, 1 and 2 as significant to $\sigma_{\gamma\gamma}$, a comparison with measured cross-sections results in A = 275 nb and B = 300 nb·GeV [34]. These values were used for this work as they have been found by previous experiments [16, 18].

The first two terms describe how $\sigma_{\gamma\gamma}$ varies with momentum transfers Q_i^2. The quantity F_{VDM} is the VDM form factor. However, F_{VDM} is here taken from the **Generalised VDM model (GVDM)** since this model also takes into account effects from the higher mass resonances and the continuum. It is given by [35] as

$$F_{VDM}(Q^2) = \sum_{V=\rho,\omega,\phi} r_V \frac{1 + Q^2/4m_V^2}{(1 + Q^2/m_V^2)^2} + \frac{0.22}{1 + Q^2/m_0^2} \tag{2.10}$$

Here m_0 = 1.4 GeV and m_V denotes the mass of vector meson V. The factors r_V are related to the coupling between vector meson V and the photon. The following r_V-values were used [27]: r_ρ=0.65, r_ω=0.08 and r_ϕ=0.05.

$\sigma_{\gamma\gamma}^{VDM}$ varies with p_T^2 as

$$\frac{d\sigma_{\gamma\gamma}^{VDM}}{dp_T^2} \sim \frac{1}{e^{ap_T}} \tag{2.11}$$

This exponential behaviour leads to a suppression of high-p_T VDM events.

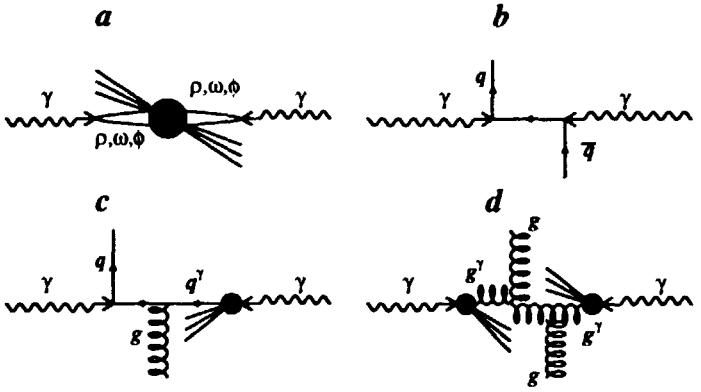

Figure 2.3: Diagrams which are contributing in lowest order to the two-photon multi-hadronic system X. (a) VDM contribution, (b) QPM contribution, (c) and (d) examples of singly and doubly resolved QCD-RPC contributions.

2.1.5.2 The QPM Model

From other experiments it is known that photons can exhibit pointlike coupling directly to a quark-antiquark pair ($e^+e^- \rightarrow e^+e^- + q\bar{q}$), which subsequently fragments into hadrons. The resulting events show typical two-jet topologies. This lowest order Born procedure is modelled by the perturbative **Quark Parton Model (QPM)** (Figure 2.3.b). Contrary to VDM, QPM is only applicable at large Q^2 or high quark p_T. In these regions the interaction times are too short for the formation of bound states. The dominant scale for the QPM model is p_T^2, meaning that $p_T^2 > Q^2$ for the QPM case.

The QPM contribution $\sigma_{\gamma\gamma}^{QPM}$ to the total cross-section is in general comparatively small at the relatively low Q^2 of most two-photon events. However, at large Q^2 the influence of the QPM process becomes significant. A full calculation of $\sigma_{\gamma\gamma}^{QPM}$ for hadron production is rather complicated, involving the sum of several terms [27]. Refer to the sub-chapter on Cross-Sections above for further details. The QPM W dependence in lowest order is found to follow

$$\sigma_{\gamma\gamma}^{QPM} \sim \frac{1}{W^2} \tag{2.12}$$

while the p_T^2 dependence is given by

$$\frac{d\sigma_{\gamma\gamma}^{QPM}}{dp_T^2} \sim \frac{1}{p_T^4} \tag{2.13}$$

By comparing (2.11) and (2.13), it is seen that the QPM hard scattering processes become dominant above around p_T >1 GeV. This p_T limit and the involved energies are quite small compared to other reactions. Two-photon events thus allow clean, low-energetic studies of hard scattering processes.

2.1.5.3 The QCD-RPC Model

Apart from the QPM model, generating two-jet events, other hard scattering multi-jet diagrams are possible. For the case $p_T^2 > Q^2$, where Q^2 is very small, these diagrams start to dominate. Their contributions are described by the **QCD Resolved Photon Contribution (QCD-RPC)** model. Two cases are possible: single resolved (Figure 2.3.c) and double resolved (Figure 2.3.d) diagrams. By resolved is meant that one, or both, of the photons are resolved into its (their) hadronic constituents. The resulting particles produce (together with the normal two jets) so-called remnant jets. The QCD-RPC model thus generates three-jet and four-jet events. However, the remnant jets are mainly produced at very small angles relative to the beams, making them difficult to detect. The bulk of the visible QCD-RPC events will therefore be seen to have a similar high-p_T two-jet topology as the QPM events.

The single resolved QCD-RPC contribution contains two sub-processes, $\gamma g \rightarrow q\bar{q}$ and $\gamma q \rightarrow gq$, while the double resolved one contains eight $(q, \bar{q}, g)$ sub-processes. Here g means a gluon, while q ($\bar{q}$) is a quark (antiquark). These sub-processes allow experimental tests of the theoretical predictions for the photon quark and gluon densities.

Important ingredients in cross-section calculations involving incoming particle hadronic structures, such as the QCD-RPC model, are the **Parton Density Functions (PDF)**. The variable X is here defined as the fraction of the total hadron longitudinal momentum carried by a given parton (q, $\bar{q}$ or g). The PDF's give, for each parton, the parton density for a given (X,Q^2)-value, where Q^2 is the momentum transfer. This is needed in perturbative QCD calculations as they solve the Altarelli-Parisi equations to describe the Q^2 dependence of the parton densities.

There are several different PDF sets available, though some of them are not applicable for two-photon studies since they are derived from deep inelastic $e\gamma$ experiments at high Q^2. Experimental results are needed to differentiate between the PDF's. A free parameter for each PDF is its p_T^{min}-value, *i.e.* the minimum transverse momentum required for the associated QCD-RPC process to take place. Since these processes are perturbative, such a p_T-cut is required to stay above the non-perturbative VDM region to avoid event double-counting. The p_T^{min}-values are constrained by the visible cross-sections. Normal values vary between 1.5 and 3.0 GeV, depending on the actual PDF set. The PDF's are finally compared by studying key physical distributions (*e.g.* W, p_T^{jet} *etc*).

The cross-section calculations for the single and double resolved QCD-RPC processes are seen above to be dependent on the PDF. The resulting calculations are outside the scope of this work; an overview over the calculations for some different PDF sets is given by [27]. Asymptotically, the QCD-RPC cross-section is found to have a similar p_T^{-4}-behaviour as for the QPM case (2.13).

2.2 Two-Photon Physics at DELPHI

Two-photon physics at DELPHI have, so far, been studied in the single-tagged and no-tagged modes. Double-tagged event studies will also be performed once the LEP integrated luminosity is large enough for having a significant data sample.

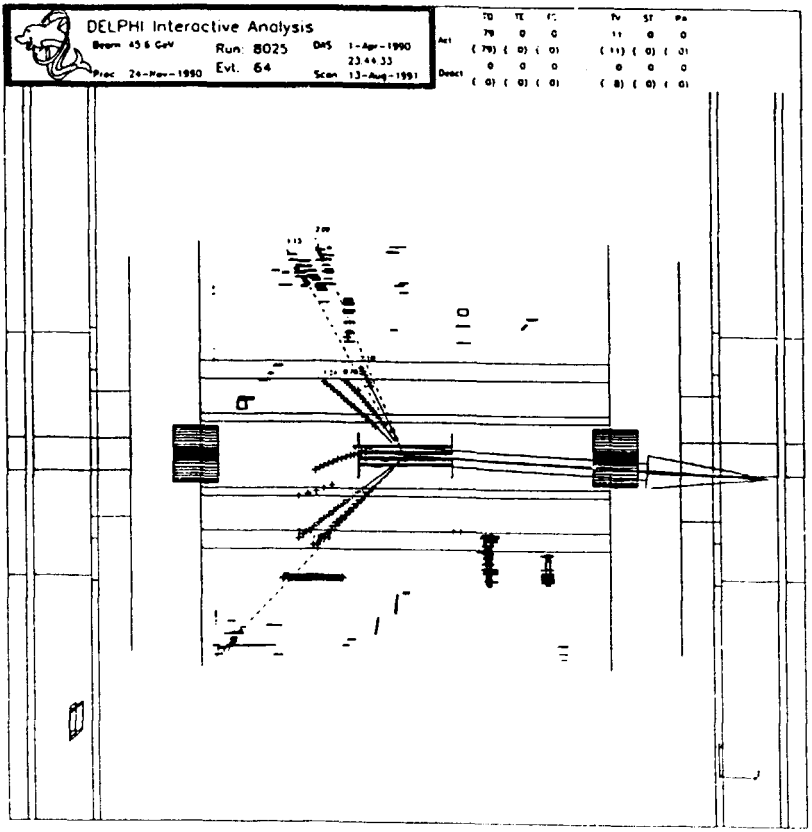

Figure 2.4: Longitudinal event display of a two-photon event as seen by the DELPHI detector. The arrow represents the calculated missing momentum.

DELPHI allows two-photon tagging inside a large Q^2-range through its three forward electromagnetic calorimeters. Different aspects of the photon can therefore be studied. High-Q^2 events are used for testing deep inelastic scattering theory, while perturbative QCD resolved photon processes can be studied by low-Q^2 events. At DELPHI, the latter can be studied both in the single-tagged and no-tagged modes. Different DELPHI tagging parameters are given in the table below. Figure 2.4 show a longitudinal event display of a two-photon event as seen by DELPHI [27].

Main parameters for the different DELPHI two-photon tagging cases.

Tagger	θ [mrad]	$< Q^2 >$ [GeV^2]	$\int\mathcal{L}$ [pb^{-1}]	#ev.	σ [pb]	Backgr. [%]
FEMC	175 - 637	80	61	100	1.7	7
SAT	43 - 135	12	26	300	12	5
VSAT	5 - 13	0.06	28	500	17	4
(no tag)	<43	0.12	32	18000	570	3

The table illustrates clearly how the two-photon cross-section increases for low Q^2. The different integrated luminosities ($\int\mathcal{L}$) reflect which data have been included in the corresponding analyses (FEMC: 1991-93, SAT and VSAT: 1991-92, no-tag: 1990-92). Reasonably low background levels are also seen, independently of tagging case. The no-tag events are anti-tagged by SAT and FEMC, but not by VSAT. This results in VSAT-tagged events, which lie inside a very narrow Q^2-range, having a smaller $< Q^2 >$ than no-tagged events.

An overview over two-photon physics at DELPHI is given in Appendix B. Below will first be given a very brief description over the results obtained from FEMC- and SAT-tagged data, after which follows a more detailed discussion of two-photon physics with VSAT-tagged data. This is also described in Appendix C. Finally follows a short section on the results of the no-tag analysis.

2.2.1 Results of FEMC- and SAT-Tagged Data Analyses

For the FEMC- and SAT-tagged cases, having rather large $< Q^2 >$ of 80 and 12 GeV^2 respectively, the two-photon process can be viewed as deep inelastic scattering of electrons off quasi-real photons. This approach assumes the non-tagged photons to have negligible momentum transfers, which is assured by anti-tagging requirements. Simulation studies showed these momentum transfers to have an average value of around 0.1 GeV^2 for the SAT-tagged case.

A VDM+QPM model was found [36, 37] to fully describe the data for both the FEMC- and SAT-tagged cases. In the description of the QPM model, it was stated that the relative weight of QPM increases with $< Q^2 >$. A simulation study of $R = \sigma_{QPM}/(\sigma_{VDM} + \sigma_{QPM})$ illustrates this, SAT here having $R = 58\%$ and FEMC $R = 81\%$. This should be compared to QPM influences of around 10% for the low-Q^2 cases.

Work is currently in progress to unfold the FEMC- and SAT-tagged data to be able to study the photon structure function F_2^γ.

2.2.2 Results of VSAT-Tagged Data Analyses

Results of VSAT-tagged two-photon data analyses have been reported at the HEP 93 conference ([38] and Appendix B) and in a forthcoming *Physics Letters B* article (Appendix C). The latter gives a detailed description of the simulation methods, event selection cuts, background rejection procedures *etc* that were used for analysing the VSAT-tagged events. This will not be repeated here, emphasis instead being put on a rather thorough discussion of the main results available so far. Appendix C should therefore be read in conjunction with the text below to obtain a complete picture of the VSAT-tagged two-photon data analyses.

Comparing the VDM+QPM model with VSAT-tagged data reveals the simulated cross-section to be too small to explain the data. The shapes of relevant physics histograms are also seen to differ from the data distributions. However, there is a large theoretical uncertainty in the calculation of the VDM cross-section. A study was carried out to investigate if increasing the VDM cross-section would result in a better agreement with data.

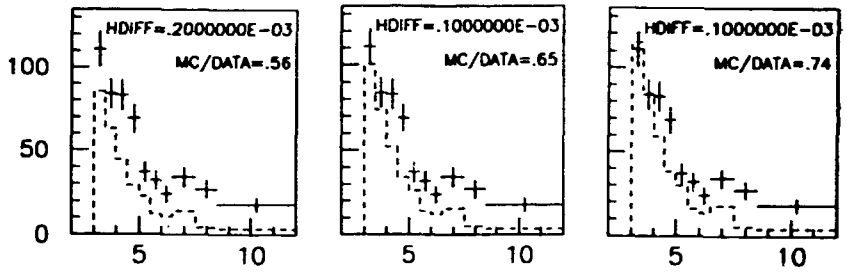

Figure 2.5: Three histograms showing comparisons between the number of events in VSAT-tagged data and the VDM+QPM model *vs.* $W_{visible}$ [GeV]. The VDM cross-sections are multiplied by 1.0, 1.2 and 1.4 respectively.

Figure 2.5 shows three histograms over number of events *vs.* $W_{visible}$ [GeV]. The VDM+QPM predicitions are represented by hatched lines while the data are shown with error bars. Below each histogram is indicated the relevant VDM cross-section multipliers, increases of 0%, 20% and 40% being tested here. The MC/DATA ratios compare simulated and data cross-sections by dividing the corresponding number of events. Without any VDM increase only 56% of the data cross-section is reproduced by the VDM+QPM model, while even a rather large (40%) VDM increase leads to the data having 26% more events than the model.

The shapes of the VDM+QPM and data distributions of Figure 2.5 were compared using the HDIFF statistical test algorithm included in the HBOOK program package [39]. A Kolmogorov test [40] is performed on the distributions, resulting in a returned HDIFF value between zero and one. The higher the value, the higher the compatibility between the tested distributions. Very low HDIFF values are shown in Figure 2.5, confirming the visibly large differences between the VDM+QPM and data distributions independently of VDM cross-section multiplier. Comparing the first and last histograms, the larger VDM cross-section is seen to result mainly in more low-$W_{visible}$ events as given by equation (2.9). The VDM+QPM model is

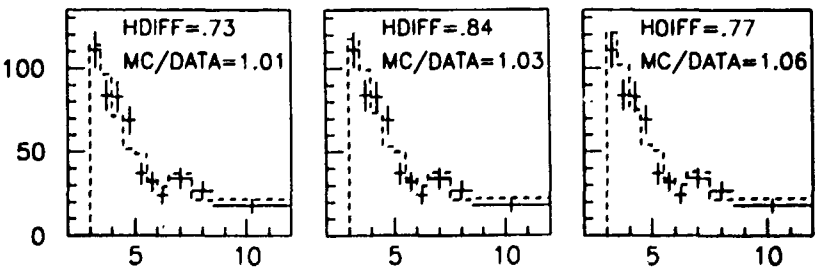

Figure 2.6: Three histograms showing comparisons between the number of events in VSAT-tagged data and a full VDM+QPM+(QCD-RPC) model *vs.* $W_{visible}$ [GeV]. The VDM cross-sections are multiplied by 1.0, 1.05 and 1.1 respectively.

thus seen to be inadequate, even when appreciable VDM cross-section increases are applied.

Figure 2.6 also shows three $W_{visible}$ histograms, but with a QCD-RPC component being added (*i.e.* the full VDM+QPM+(QCD-RPC) model). The included QCD-RPC parton density function is here the one according to M. Drees and K. Grassie (DG) [41], with p_T^{min}=1.45 GeV. Subsequent tuning of p_T^{min} have resulted in an optimum value of 1.56 GeV for DG. The VDM cross-section multipliers in this figure corresponds to increases of 0%, 5% and 10%. All three histograms are now seen to be compatible with the data, a 5% VDM cross-section increase leading to the best result with MC/DATA=1.03 (*i.e.* 3% too many simulated events) and HDIFF=0.84. The inclusion of the QCD-RPC model is thus seen to strongly improve the description of the experimental data.

Many histograms over VSAT-tagged data are given by Appendix C, but in addition Figure 2.7 and Figure 2.8 contain some of the main results obtained. These histograms were presented at the HEP 93 conference (Appendix B). Individual model behaviours are included in the first three histograms, with QCD-RPC abbreviated to QCD. The included parton density function is also here DG for all histograms, again with a p_T^{min}-value of 1.45 GeV.

The upper histogram of Figure 2.7 shows the number of charged tracks *vs.* inclusive charged p_T^2. The VDM part, though large at low p_T^2, is seen to diminish rapidly with increasing p_T^2 and is negligible above p_T^2=2 GeV^2. The QPM model is about an order of magnitude smaller at low p_T^2, but the comparatively weak decrease with increasing p_T^2 makes QPM dominate over VDM at large p_T^2. However, the summed VDM+QPM model is seen to fail to describe the data. The large deficit of simulated tracks at low p_T^2 corresponds to a too low model cross section, while the too strong VDM+QPM decrease for larger p_T^2 do not follow the shape of the data. The QCD-RPC contribution is seen to be of approximately the same magnitude as the VDM model at low p_T^2, but has a more gentle decrease for larger p_T^2. It is instructive to compare the relative p_T^2 behaviours of these models to the $d\sigma_{\gamma\gamma}/dp_T^2$ relations given in the chapter on Theoretical Background. Finally, including also the QCD-RPC contribution into a full VDM+QPM+(QCD-RPC) model, data is seen to be well-described both concerning cross section and overall p_T^2-dependence.

The $W_{visible}$ spectrum is shown in the lower histogram of Figure 2.7. The VDM+QPM model is again seen to have difficulties describing the data, a too small cross section and a lack of events above $W_{visible}$=8 GeV being apparent. Adding also the QCD-RPC model results in a good agreement with data. Notice how QCD-RPC processes become dominant for $W_{visible}$ >5 GeV.

Figure 2.8 (upper histogram) shows the distribution of the beam-normalised tag energy E_{tag}/E_{beam}, with E_{tag} measured by the VSAT. Data is again seen to require the full three-component model. This histogram being drawn in a linear scale, the relative contributions of the different models can be estimated from the areas under their corresponding curves. As expected for low-Q^2 data, the contribution from the QPM process is quite small (~10%). The VDM and QCD-RPC contributions are seen to be approximately equal in magnitude. While the peak around E_{tag}/E_{beam}=0.9 is due mainly to VDM contributions, QCD-RPC processes are seen to dominate for E_{tag}/E_{beam} <0.8

Observing the above QCD-RPC dominated regions, the lower plot of Figure 2.8

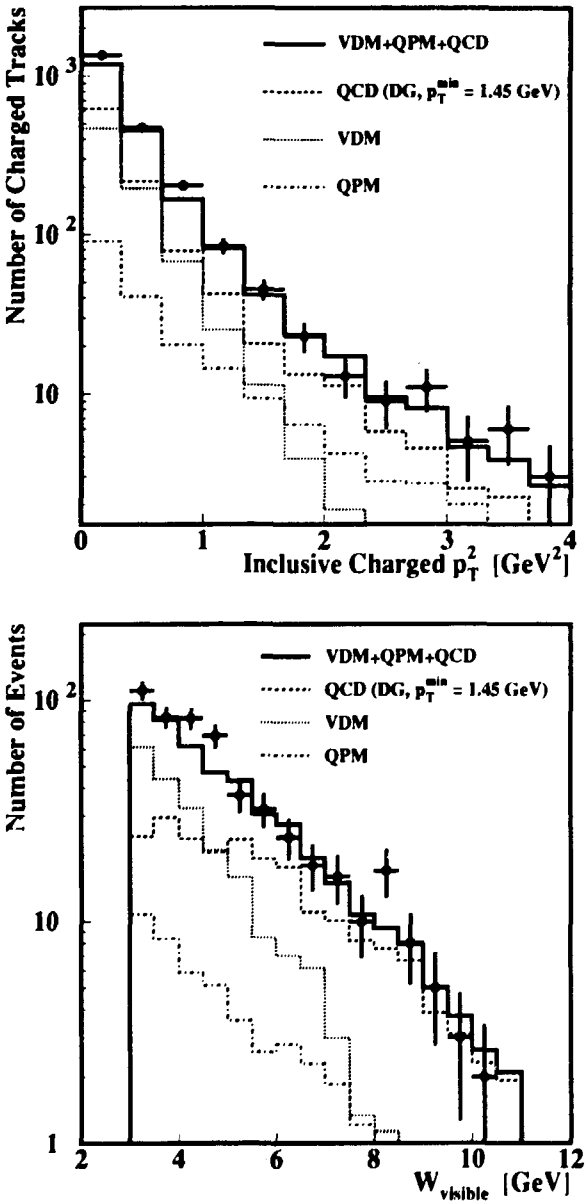

Figure 2.7: Both histograms show comparisons between VSAT-tagged data and a full VDM+QPM+(QCD-RPC) model. Individual model behaviours are also indicated. The upper histogram shows inclusive charged p_T^2, while the lower one shows $W_{visible}$.

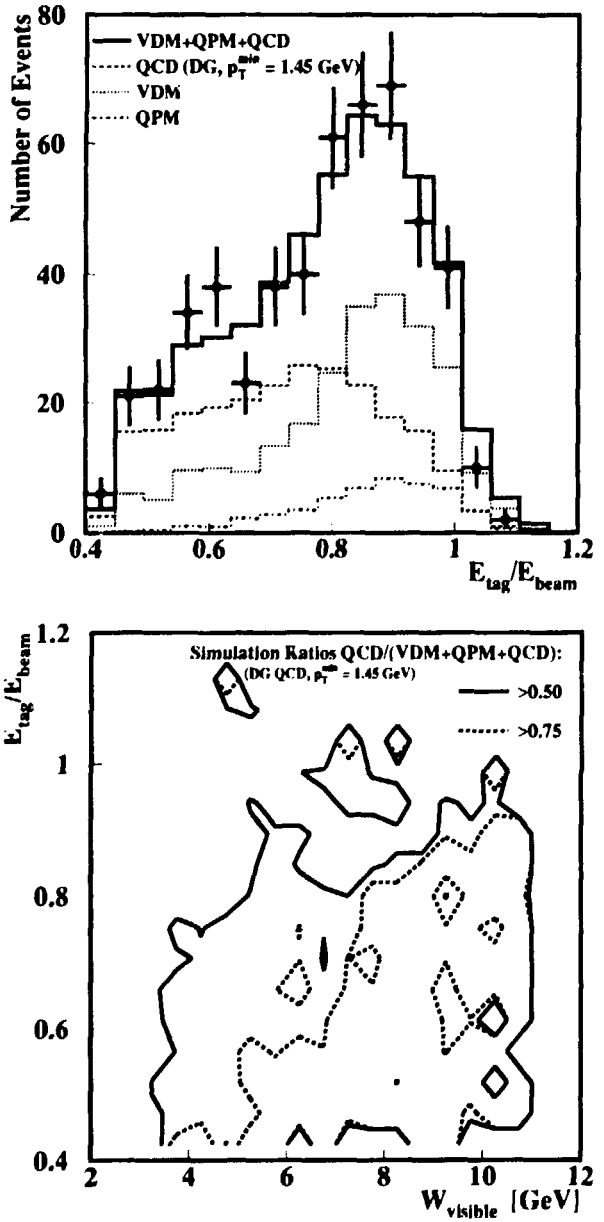

Figure 2.8: The upper histogram shows a comparison between VSAT-tagged data and a full VDM+QPM+(QCD-RPC) model for E_{tag}/E_{beam}. Individual model behaviours are also indicated. The lower histogram shows, for simulated VSAT-tagged data, the influence of the QCD-RPC component in the E_{tag}/E_{beam} *vs.* $W_{visible}$ plane. QCD-RPC contributions of 50% and 75% are indicated.

is a two-dimensional contour histogram of E_{tag}/E_{beam} *vs.* $W_{visible}$. Only simulated data are used in this figure. The bins are filled with the number of QCD-RPC events normalised to the number of events of the full three-component model, *i.e.* the ratio (QCD-RPC)/(VDM+QPM+(QCD-RPC)). Two contours are shown: those corresponding to 50% and 75% QCD-RPC contributions. Ignore the small 'islands' in this plot, they are due to low statistics in some bins. This plot suggests a method of isolating an event sample dominated by QCD-RPC processes by introducing cuts in the E_{tag}/E_{beam} *vs.* $W_{visible}$ plane. Initial tests show that requiring a 50% QCD-RPC contribution rejects about half the initial two-photon event sample, a more strict 75% requirement of course leaving still fewer events to study. Due to the at present rather limited VSAT-tagged two-photon event sample (~500 events), this method of selecting QCD-RPC events will be pursued when more data have been collected.

Having shown the need for QCD-RPC processes to describe the VSAT-tagged data, several different parton density functions (PDF) are available for inclusion in the simulations [42]. Five PDF's have so far been simulated and compared with the data. Two of them, that of D.W. Duke and J.F. Owens (DO) and set 3 of A. Levy, H. Abramowicz and and K. Charchula (LAC3), where found to be incompatible with the data. Differentiating between the other three simulated PDF's, those of L.E. Gordon and J.K. Storrow (GS), DG and set 1 of LAC (LAC1), will require a larger data sample than presently available. Refer to Appendix C for a detailed description of the PDF *vs.* data comparisons.

2.2.3 Results of No-Tagged Data Analyses

Analyses have been performed also with DELPHI no-tagged data [43], *i.e.* with data showing similar low-Q^2 and low-$W_{visible}$ characteristics as the VSAT single-tagged data. The results of the two analyses support each other.

No-tag data were also found to require QCD-RPC processes in order to describe the cross-section and distributions of data. Tests of different parton density functions were carried out by analysing an event sample containing high-p_T jets. The DO and DG PDF's were found to be worse than GS and LAC1 when compared to data.

Chapter 3

Online Beam Monitoring

By an online beam monitoring system is meant a real-time system providing fast response to changing beam parameters. We will here consider the case of monitoring beam conditions at the interaction points of an electron-positron collider.

Real-time knowledge of beam parameters is essential for several reasons. The accelerator physicists need to know how the experiments react to different machine set-ups. They can then tune their accelerator for optimum physics conditions at the interaction points. The particle physicists, having sensitive detectors, need to know the beam conditions to see when they are good enough to start taking data.

In this chapter the main beam parameters of interest to a particle physicist is first introduced, after which the DELPHI system for online monitoring of these is briefly described. This system is treated at length in Appendix D. The features of the VSAT online detector and beam monitoring program **VSAT_MONITOR** is then thoroughly discussed. Finally, a short summary of VSAT measurements of a LEP beam separation scan is given. A more complete discussion is found in Appendix E.

3.1 Main Beam Parameters

From an accelerator physicist's point of view there are many parameters which must be monitored in order to run the machine efficiently. The special devices needed for this task, called beam instruments, are often tailor-made to the accelerator [44]. However, for the particle physicist usually only a few of the main machine parameters are of interest: the luminosity, the background and the beam spot.

3.1.1 Luminosity

A key parameter of any accelerator is its luminosity, which is a measure of the machine's ability to produce particle reactions. The concept of luminosity will first be defined for LEP-like conditions, after which follows a brief description of the Bhabha scattering process which is used for luminosity determination.

3.1.1.1 Definition of Luminosity

Consider the case of an electron-positron collider having its beam particles divided into bunches of the same transverse dimensions. Assuming the beams collide

without any relative incident angle, the counting rate per unit time $dN_{\mathcal{P}}/dt$ of a specific process $\mathcal{P}$ one observes is then given by [45]

$$\frac{dN_{\mathcal{P}}}{dt} = \frac{f\,N^+\,N^-}{2k}\,\frac{\sigma_{\mathcal{P}}}{2\pi\,\sigma_x\,\sigma_y} \tag{3.1}$$

Here f is the particle revolution frequency and $N^+\,(N^-)$ is the number of positrons (electrons) in the beam. k is the number of particle bunches per beam, leading to $2k$ interaction points around the machine. The probability of the observed reaction $\mathcal{P}$ to occur is called its cross-section $\sigma_{\mathcal{P}}$ and has the dimension of area. The horisontal and vertical transverse beam dimensions are given by σ_x and σ_y. The last denominator thus gives the cross-sectional area under which the beams collide.

It is more common to talk about rates in terms of beam currents I^j, defined by $I^j = N^j\,e\,f$. Here j is either + or − and e is the electron charge. Equation (3.1) can then be rewritten

$$\frac{dN_{\mathcal{P}}}{dt} = \frac{I^+\,I^-}{e^2\,f\,2k}\,\frac{\sigma_{\mathcal{P}}}{2\pi\,\sigma_x\,\sigma_y} \tag{3.2}$$

The luminosity $\mathcal{L}$ is defined by

$$\mathcal{L} \equiv \frac{dN_{\mathcal{P}}/dt}{\sigma_{\mathcal{P}}} \tag{3.3}$$

while the totally delivered luminosity during a certain time interval (*e.g.* a fill), the integrated luminosity $\bar{\mathcal{L}}$, is defined through

$$\bar{\mathcal{L}} \equiv \int \mathcal{L}\,dt = \frac{N_{\mathcal{P}}}{\sigma_{\mathcal{P}}} \tag{3.4}$$

Knowing the luminosity to a high precision is crucial to any particle physics experiment as it, through (3.4), relates the number of detected events N of some interesting reaction (*e.g.* hadronic Z^0 decays) in a certain time to its cross-section, which is often to be found. All data are therefore normalised to the integrated luminosity during which they were taken.

The luminosity of a collider can be found directly by measuring its beam currents I^j and using (3.2) and (3.3). However, the accuracy of this method is too low for high-precision experiments. Instead one normally calculates the luminosity at an interaction point indirectly by measuring the reaction rate of a special process with a known cross-sectic... This luminosity-calculation process should fulfill the following requirements:

- It should have a comparatively large visible, *i.e.* detectable, cross-section for minimising the statistical error of the measurement. Ideally the cross-section of the luminosity process should be several times that of the physics reactions of interest.
- It should be well-known in order to minimise the systematical error of the measurement. This means both accurately knowing its cross-section and the acceptance of the experimental set-up.

- It should have a high signal-to-noise ratio, again to minimise the systematic error of the measurement. The process should be chosen so that interfering background sources are easily rejectable.

3.1.1.2 The Bhabha Scattering Process

At virtually all electron-positron colliders one has chosen the Bhabha scattering process [46] as luminosity calculation process. The electrons and positrons here undergo elastic scattering against each other, *i.e.* $e^+ + e^- \rightarrow e^+ + e^-$ (Figure 3.1).

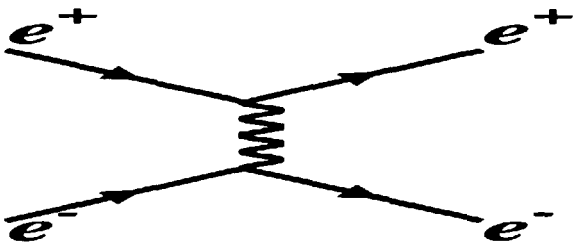

Figure 3.1: The Bhabha scattering process in lowest order QED.

In a lowest order QED approximation the scattered particles have the same energy, but opposite azimuthal and polar angles. A precise luminosity measurement requires that also different weak and radiative processes are taken into account for calculating the Bhabha cross-section [47, 48]. However, for the precision required of an online beam monitoring system, only the lowest order QED process needs to be taken into account, since at high energies and small polar angles the neglected higher order terms are only a factor 10^{-5} of the lowest term [49].

The lowest order QED differential cross-section for the special case of Bhabha scattering into very small polar angles θ at high centre-of-mass energies $\sqrt{s}$ is [48]

$$\frac{d\sigma}{d\Omega} = \frac{4\alpha^2}{s}\frac{1}{\theta^4} \tag{3.5}$$

Here $d\Omega$ is the solid angle element and α is the fine-structure constant. The sharply falling distribution of Bhabha scattered particles with polar angle is evident. Placing detectors closely around the beam pipe thus optimises the yield of Bhabha scattered events.

3.1.2 Background

Ideally, the beam particles in an electron-positron collider circulate in perfect vacuum around a closely defined orbit, each particle having the same energy. In reality this is not true as there also always exists lower momenta beam particles which needs to be rejected by the physics experiments [50]. Beam particles can lose momenta mainly through two processes. Though both involve the acceleration of charges, one normally refers to Bremsstrahlung for motion through matter and

synchrotron radiation for circular acceleration. These processes limit the life-time of the circulating beams.

3.1.2.1 Bremsstrahlung Off-Momentum Beam Particles

Even though the vacuum in the beam pipe might be good there always remain some gas molecules. The nuclei of these molecules can interact electromagnetically with the beam electrons and positrons, bending their trajectories. This acceleration causes photons to be emitted. The process is called Bremsstrahlung [51].

The energy loss of beam particles due to Bremsstrahlung can be considerable, around several GeV, giving rise to beam particles being strongly off-momenta with respect to the nominal value. Most of them go forward, into small polar angles, creating a type of envelope around the beams, and they are thus mainly seen by detectors in the forward direction. The photons mainly go undetected into the beam pipe. When Bremsstrahlung processes occur near the interaction points the photons can be seen by the central tracking devices. The amount of observed background depends on how good the vacuum is around the interaction region.

3.1.2.2 Synchrotron Radiated Photons

Around an electron-positron collider there are several magnets used for beam transport, orbit correction and squeezing. The beam particles emit photons, so-called synchrotron radiated photons, when being accelerated by these magnetic fields [52]. The photon energies are only a few hundred keV. The magnets in the sections around the interaction points can produce photons which are seen principally by the central tracking detectors. The energy losses of the electrons and positrons are small enough to be mostly insignificant, hence there is no beam loss due to this.

3.1.3 Beam Spot

By beam spot is meant the envelope created by the vertices, *i.e.* the exact volume in space at which the beam particles collide. The nominal vertex is designed to be concident with (x, y, z)=(0,0,0) in the detector coordinate system. Due to variations in beam parameters, anomalous situations, alignment problems *etc.* this is not always the case in reality, necessiating beam spot monitoring. Though the precision of an online measurement need not be very high, some (offline) physics analyses require good knowledge of the beam spot.

3.2 The DELPHI Online Monitoring System

A purpose-made system exists for information exchange between the LEP accelerator and the physics experiments [53]. The former provides data on LEP beam currents, collimator settings *etc.* while the experiments measure luminosity, background *etc.* at their interaction points. At the DELPHI experiment the data are available for display [54] as well as logged to a database [55]. The DELPHI online monitoring system, which is fully described in Appendix D, has been used in joint

LEP-DELPHI investigations to optimise the beam conditions at the DELPHI interaction point [56]. Parts of the system hardware and software are also described in [57] and [58]. Some parts of the system have recently been updated to increase speed and reliability [59].

Several DELPHI sub-detectors participate in the online monitoring system in order to have a complete and redundant picture of the beam conditions. Thus luminosity is measured by SAT and VSAT, synchrotron radiated photons are measured by ID and TPC while all of them, as well as special Radiation Monitors (RM), measure off-momentum beam particles.

Some SAT and VSAT signals, and all the RM signals, are always available independently of the DELPHI data acquisition system. The TPC signals and some ID signals also become available when their high-voltages are turned on. When the DELPHI data acquisition is finally running all the monitoring signals are available.

The available signals at a given time are thus dependent on the current beam conditions. This is displayed by Figure 3.2, showing DELPHI online monitoring for the beginning of a LEP fill. The top histogram (VSAT BKGD1) is a measure of the VSAT off-momentum beam particle trigger rate. The second histogram (VSAT TRIGGER LUM.) shows the VSAT Bhabha trigger rate, which is proportional to luminosity. Since SAT is the main luminosity detector of DELPHI, this rate is scaled to the SAT-calculated luminosity. Both these VSAT signals come directly from its local trigger, and they are therefore always available. Histogram three (TPC BKGD2) is proportional to the total counting rate of the TPC wires, *i.e.* proportional to both synchrotron photons and off-momentum beam particles. The luminosity given by the SAT online monitoring program (SAT ONLINE LUM.) is displayed in the fourth histogram. This signal is available only when DELPHI is taking data. All histograms show rate or luminosity along the vertical axis and time along the horisontal axis.

Below is a description of what is seen in Figure 3.2. The letters **A** to **F** refer to those along the bottom of the figure, indicating at what time some operation was carried out.

- **A** No beams in LEP.
- **B** Particles are injected into LEP. The beams are rather 'dirty' as can be seen from the high VSAT BKGD1 rate. The low VSAT TRIGGER LUM. values indicate that the beams are circulating with very few collisions.
- **C** VSAT TRIGGER LUM. rises steeply, meaning the beams have correct energy and are brought into collision. Some further beam tuning is performed as VSAT TRIGGER LUM. continues to increase slowly. VSAT BKGD1 is still high.
- **D** The collimators are moved into their correct positions. This is monitored by VSAT BKGD1 as a sharp decrease in background.
- **E** The VSAT BKGD1 background is considered low and stable enough for the DELPHI operators to turn on the TPC high-voltages. TPC BKGD2 then goes up to a stable value.
- **F** Both VSAT BKGD1 and TPC BKGD2 backgrounds are low and stable so the DELPHI data acquisition is started. SAT ONLINE LUM. is seen to agree well with VSAT TRIGGER LUM.

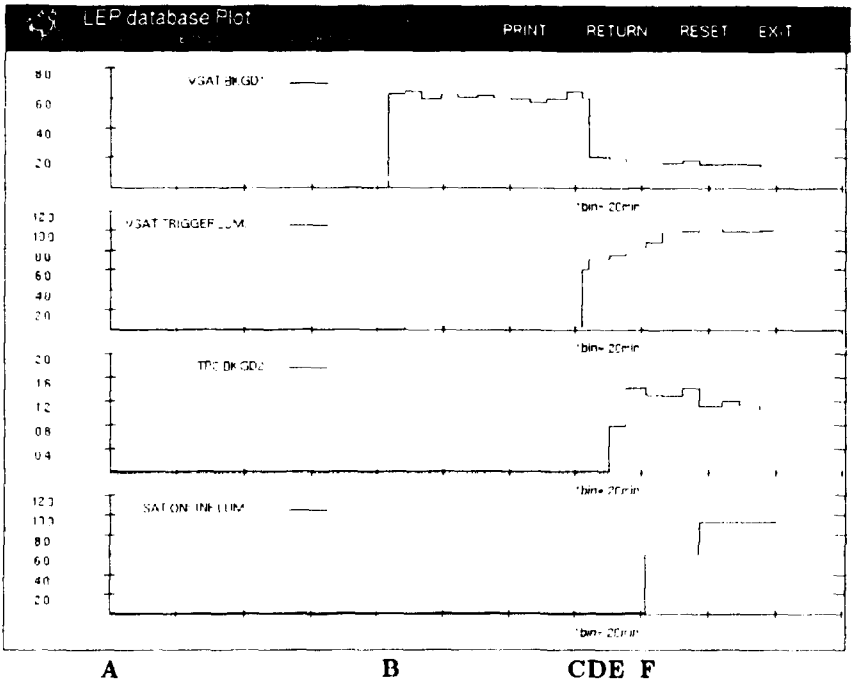

Figure 3.2: DELPHI online monitoring of the beginning of LEP fill 1456. The data were picked up from the database. The figure is described in the text.

3.3 The VSAT Online Monitoring Sub-System

Due to the VSAT coverage of very small polar angles, *i.e.* being placed close to the beam pipe, it can provide useful information on different beam parameters. Online beam monitoring was originally the main reason for constructing the VSAT. Several VSAT signals are available online, some of them independently of the DELPHI data acquisition.

Both DELPHI-gated and ungated signals are sent directly from the local VSAT trigger. They give information on off-momentum beam particle background, Bhabha scattering events (for luminosity determinations) and background to the Bhabha events. The signals are available together with a bunch counter, making studies of individual LEP particle bunches possible. The VSAT trigger signals are described in detail in Appendix D, and they will not be further discussed here.

DELPHI-gated online signals are also available from the VSAT online monitoring program, `VSAT MONITOR`, which is decribed below. This program, running on

the VSAT-specific equipment computer, analyses the sample of VSAT data made available for monitoring by the DELPHI data acquisition system [60, 61, 62, 63]. Then follows a performance test of the VSAT_MONITOR routines, where comparisons are made with online and offline results from different DELPHI and LEP detectors. VSAT raw data files were moved to the DELPHI online cluster for some of these comparisons. VSAT_MONITOR was then set up to run in a so-called playback mode (see details below).

3.3.1 The VSAT_MONITOR Program Package

The main purpose of an online monitoring program is to immediately spot any errors in the detector's data stream. It can also supervise the general status of the detector, detecting changes in pedestal values *etc.* Some detectors can also directly, through its online monitoring program, provide useful physics results by rapidly analysing the data as they are taken. All these tasks are performed by the VSAT online monitoring program package, called VSAT_MONITOR, consisting of around 6000 lines of FORTRAN code and 1000 lines of DCL command language code. It provides both interactive and non-interactive monitoring of the VSAT [64].

Interactive monitoring of individual data buffers, which for the VSAT normally contains a few events each, is available through event displays. The user can here either display the raw data which, for the VSAT, are packed in hexadecimal format or in the final unpacked, pedestal-subtracted and calibrated format. A graphical event display have also been available, showing profiles over all data channels together with trigger information (see Appendix A, Figure 5 or Appendix E, Figure 2). It is also possible to interactively access the run-integrated histograms produced by the non-interactive task (see below) through a histogram presenter. Different operations can be performed on the histograms. Reference histograms, displaying how it 'should' look, are superimposed on each plot for comparison. Any number of users can run interactively, also from remote terminals. The user can select to look at data either online or offline, running the program in playback mode and analysing previously taken data from a file on the DELPHI online cluster. The user has at each level the option to print the current display.

The non-interactive VSAT_MONITOR task, running in batch mode on the VSAT equipment computer, is the main monitoring utility. It is always running when DELPHI is taking data, hibernating between runs. Each event is unpacked and decoded concerning physics data, pedestal data, trigger and error flags *etc.* In order to optimise the CPU-usage very few operations are performed on an event-by-event basis. Event data is instead stored in vectors. At certain time intervals operations are performed on these vectors. Thus every 60 seconds some vectors are normalised and histogrammed, while every 10 minutes results on LEP beam spot and luminosity are calculated and sent to the DELPHI online monitoring system.

Most of the operations are performed at the end of each run when output files are written and error checks are made. Error checking is crucial to ensure a stable VSAT performance. Checks are therefore carried out on a large number of parameters like percentage of corrupt events, trigger distributions in the four VSAT modules, mean ADC-values for the channels *etc.* Any value found to be outside the allowed range results in an error message being injected into a special error message utility, routing

the message to predefined receivers. Key data, any error messages and all delivered beam spot and luminosity values are automatically written to end-of-run summary files which are saved for reference.

VSAT_MONITOR also communicates with the VSAT online database [65]. At each beginning of a new run, **VSAT_MONITOR** reads in the current database values concerning pedestal values and channel status flags (*i.e.* which channels are considered non-functional). New pedestal values, and widths, together with new channel status flags are calculated by **VSAT_MONITOR** at certain intervals. The database update routines, which are normally hibernating, are then woken up. Any significant changes lead to updates in the database.

The global steering of **VSAT_MONITOR** is to a large extent determined by values read in from external files at each start-of-run. A user can thus decide what error checks to be made, what error limits to be allowed, what files to write *etc.*

The non-interactive part of **VSAT_MONITOR** should always be running in online mode only. However, for special sessions a user can redefine its data input area to point to a data file. This is called playback mode. The difference between the playback and online modes is that in playback mode all the data is seen by **VSAT_MONITOR**, while in online mode the data sample actually monitored depends on the CPU load of the VSAT equipment computer and the live-time of the data acquisition. During the 1991 runs about 80% of the VSAT data were monitored online. In later years practically 100% have been monitored, due to the installation of a more powerful equipment computer.

3.3.2 Event Selection

VSAT_MONITOR uses only selected and background-corrected Bhabha events for its online luminosity and beam spot analyses. The event selection criteria are broadly similar to those of the VSAT offline analysis programs. The main criteria are listed below, as are the differences from the routines on the offline level.

- The data words are first unpacked and checked for correct data format. Any corrupt or unreconstructable events are discarded.
- The analyses use only events triggered as Bhabha or False Bhabha. A False Bhabha event is defined as an accidental Bhabha coincidence, *i.e.* an event where a single hit in a VSAT module is followed by a hit in its diagonal module the next time the same two bunches collide. These events, coming from purely statistical coincidences between off-momentum beam particles surrounding the beams, indicate the background level.
- Incident (x, y)-positions are reconstructed. The online routines only find which strips were hit, and assign the centres of these strips as incident (x, y)-positions. As the strip planes have a one millimeter pitch this means a 500 μm position resolution. Special position-reconstruction algorithms are used offline, here resulting in a position resolution of 200 μm [66].
- Hits within one millimeter from any calorimeter edge are considered to have lost too much of their electromagnetic showers outside the detectors, and the event is discarded.

- A one-dimensional shower leakage correction is applied for hits with an x-position between 2 and 10 mm to the beam-pipe edge of a module. The correction, which is in the form of a pre-calculated look-up table, gives a maximum contribution of 25%. VSAT offline routines use a more exact two-dimensional correction function, taking into account also the cases of leakages close to a calorimeter corner and along the vertical (y) edges.
- Low-energetic events, with a hit having energy less than 36.5 GeV after leakage correction, are discarded. This fixed energy cut is 80% of the beam energy at the Z^0 peak. The offline energy cut was originally 80% of the actual beam energy. For later analyses this has been lowered to 70%.
- The number of False Bhabha events, which survive the above cuts, are finally subtracted. The events are then considered to be background corrected.

3.3.3 Luminosity Measurements

The precision of the VSAT_MONITOR online luminosity measurements was first tested by comparing with final SAT and VSAT offline results. SAT results were here used as reference in order to discover any VSAT-specific systematic errors. Due to statistical reasons all comparisons were carried out on a run by run basis, where each run was required to have more than 20 Bhabha events in the SAT. The average SAT and VSAT combined statistical error per run (see below) was found to be around 10%. Accepted runs needed to have both SAT and VSAT offline status flags set to zero (*i.e.* good runs). The final data sample consisted of 63 runs taken from ten LEP fills.

The upper histogram of Figure 3.3 shows, for each of the 63 runs, the ratios between the number of accepted Bhabha events by VSAT_MONITOR and by SAT offline. VSAT_MONITOR is seen to accept 18.25 times more Bhabha events than SAT, reflecting the strong forward peaking of the Bhabha cross-section (equation (3.5)). This high event rate is essential for having a reasonable statistical event sample inside the small time intervals (10 to 20 minutes) required for online monitoring purposes. Fitting a straight line to the ratios results in a χ^2 of 1.133, indicating a stable ratio between VSAT online and SAT offline Bhabha counting.

Corresponding ratios for VSAT offline and SAT offline Bhabha events are given by the lower histogram of Figure 3.3. The lower energy cut of the VSAT offline routines is here seen to lead to the slightly higher mean ratio of 19.13, while the fit results in the same χ^2-value. The Bhabha counting precision is therefore virtually identical for the VSAT online and offline programs.

Knowing the visible Bhabha cross-section is essential for a precise luminosity measurement. For the VSAT case this cross-section is quite sensitive to different beam parameters, which is corrected for at the offline level using dedicated algorithms [67, 68]. Similar corrections were also tried for VSAT_MONITOR, but they were found not to improve results since the statistical fluctuations inside a 10 min update interval are large compared to the corrections. A fixed Bhabha cross-section of 500 nb was instead used, taken as the mean value from offline results. This cross-section can vary slightly from year to year depending on the exact positions of the VSAT modules.

Figure 3.4 shows differences in luminosity values weighted by the combined VSAT

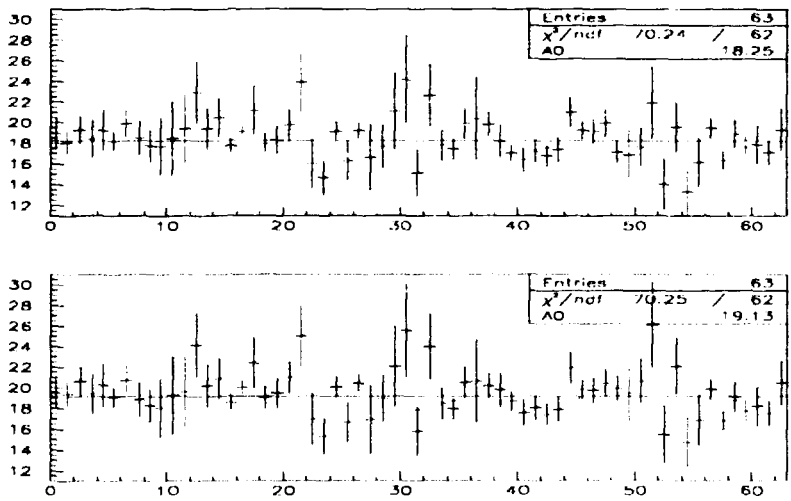

Figure 3.3: Bhabha counting ratios between VSAT online and SAT offline routines (upper histogram), and VSAT offline and SAT offline routines (lower histogram).

and SAT statistical errors, *i.e.* for each run R the histograms are filled with

$$\frac{\bar{\mathcal{L}}_R^{VSAT} - \bar{\mathcal{L}}_R^{SAT}}{\sigma^2_{comb.stat.}} \tag{3.6}$$

where the combined statistical error is given by

$$\sigma_{comb.stat.} = \sqrt{1/N^{VSAT}_{Bhabha} + 1/N^{SAT}_{Bhabha}} \tag{3.7}$$

The upper histogram compares VSAT online and SAT offline, while the lower one reflects VSAT offline *vs.* SAT offline. Using the RMS-values of Figure 3.4, estimates of the combined VSAT and SAT systematic errors of the luminosity measurements can be calculated by [69]

$$RMS^2 - 1 = \frac{\sigma^2_{comb.syst.}}{\sigma^2_{comb.stat.}} \tag{3.8}$$

The calculations give a combined VSAT online and SAT offline systematic error of (3.4±2.3)%, while the combined VSAT and SAT offline error is (2.9±2.4)%.

Again the VSAT online and offline routines give similar results, especially taking into account the large uncertainties of the systematic error estimates. These arise due to fluctuations in the comparatively small data sample tested. Knowing the systematic errors to higher precision requires using much more data, on the scale of the full DELPHI 1991 data sample. This has been performed for final VSAT offline analysis, resulting in a systematic error on the relative luminosity measurements of less than 0.2% [70].

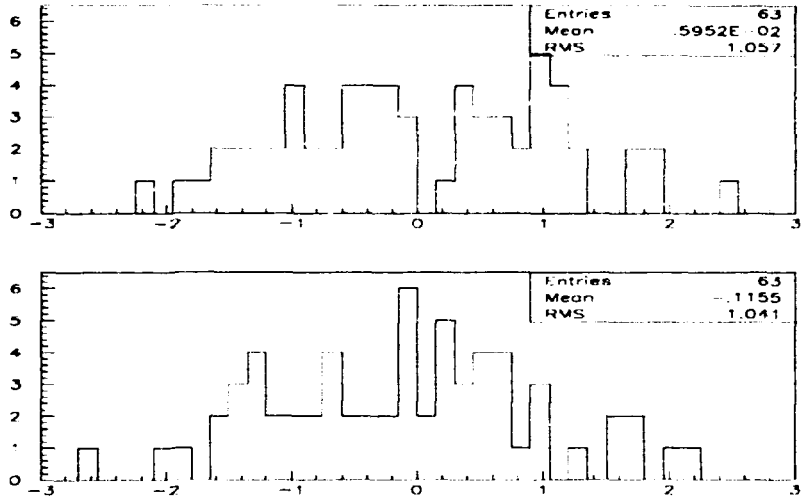

Figure 3.4: Error weighted luminosity differences between VSAT online and SAT offline (upper histogram) and VSAT offline and SAT offline (lower histogram).

The above combined VSAT+SAT systematic errors correspond to the average VSAT statistical error for a 10 minute online data sample. The accuracy of **VSAT_MONITOR** can therefore be considered adequate for the purpose of an online luminosity measurement, being much better than the required 10% error level.

Finally, **VSAT_MONITOR** luminosity calculations were compared inside a fill to those calculated by the SAT online monitoring program, which is being claimed to agree within a few percent to the SAT offline results. Data from a 1992 fill are displayed in Figure 3.5.

The upper histogram shows superimposed VSAT and SAT luminosities. SAT is the trace having wider (20 min) bins than VSAT (10 min). The lower histogram gives the VSAT/SAT luminosity ratio. A good agreement is seen between the two detectors' measurements: both respond to luminosity changes inside the fill in a similar manner, resulting in a stable ratio of around one. The peaks are due to few events inside the rather short time intervals, the SAT having about nine times less data than VSAT.

3.3.4 Beam Spot Measurements

The **VSAT_MONITOR** beam spot calculations use Bhabha events having passed the event selection criteria of Chapter 3.3.2. For each event the horisontal beam spot position (*i.e.* the x-position) is calculated by summing, with signs, the two reconstructed x-positions of the VSAT modules. This sum is proportional to the horisontal beam position. The final value is found at the end of each time interval by taking the weighted mean value of the sums in the two VSAT Bhabha diagonals.

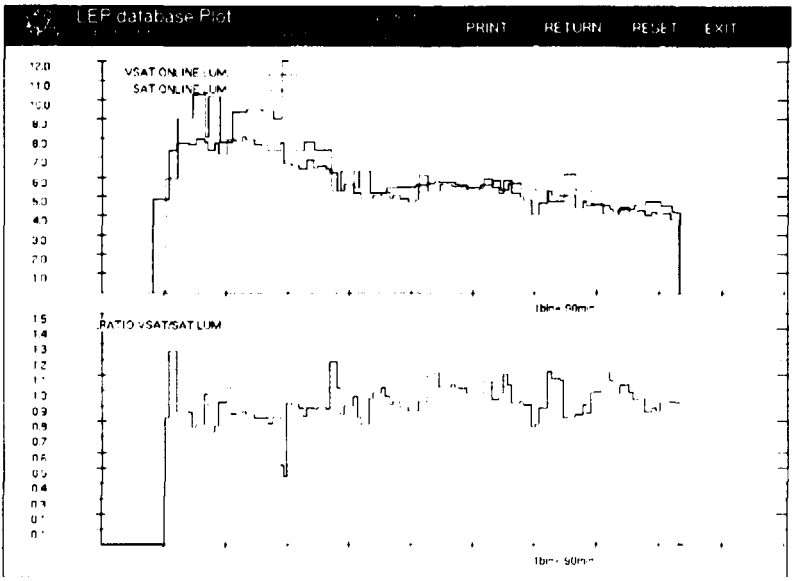

Figure 3.5: VSAT online and SAT online luminosities from fill 1456. In the upper histogram the SAT trace is the one having wider bins.

The vertical beam spot position (*i.e.* the y-position) is calculated in the same way.

The longitudinal beam spot position (*i.e.* the z-position) is found by taking instead the difference, with signs, of the above x-position sums from each VSAT Bhabha diagonal. This difference is proportional to the deviation of the longitudinal beam spot position from the nominal zero value (z=0).

Micro-Vertex beam spot data [71] were used for determining the precision of the **VSAT_MONITOR** horisontal and vertical beam spot calculations, while TPC data [72] were used for testing the longitudinal beam spot estimates.

3.3.4.1 Horisontal Beam Spot Position

Horisontal beam spot comparisons with the micro-vertex detector were done on a run-by-run basis, the only requirement being a minimum of 800 VSAT Bhabha events per run. This corresponds roughly to discarding runs shorter than 10 minutes, *i.e.* the minimum time interval used by **VSAT_MONITOR** for giving online estimates. The data sample used in the analysis consisted of 82 runs from 12 LEP fills.

Figure 3.6 shows the horisontal beam spot positions of **VSAT MONITOR** *vs.* micro-vertex data. The two measurements are seen to be correlated. Fitting a straight line to the 82 data points results in a χ^2-value of 1.178. There is an overall scale factor between the two detectors, which is due to the magnifying effects of the quadrupole magnets in the horisontal direction.

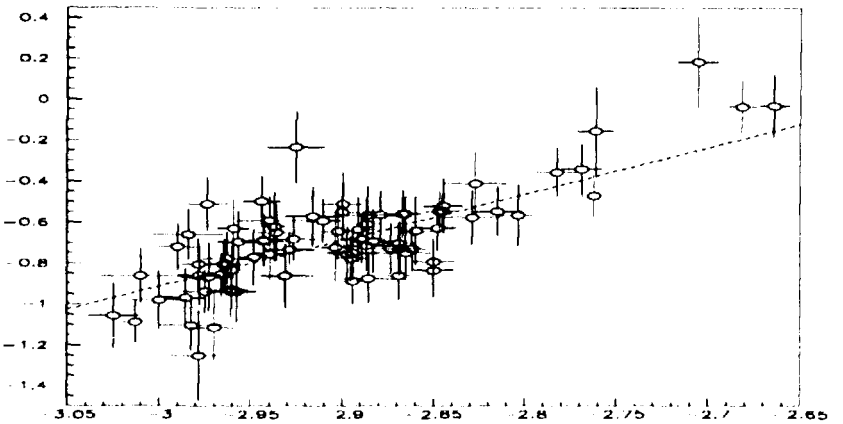

Figure 3.6: VSAT online *vs.* micro-vertex x-positions (mm).

As for the luminosity determinations, **VSAT_MONITOR** beam spot horisontal positions were plotted inside a fill (Figure 3.7). Data of the LEP Beam Orbit Measuring system (BOM) [44] were superimposed for comparison. The two overlapping curves on top of Figure 3.7 are the BOM electron and positron beam x-positions while the lower curve shows **VSAT_MONITOR** data. Apart from a scale factor the VSAT is seen to follow the BOM data. The situation in Figure 3.7 is representative of some ten other LEP fills displayed in the same manner.

Though the errors of the **VSAT_MONITOR** horisontal beam spot measurements are not comparable to those of the micro-vertex, they are still useful for online monitoring, backup measurements and alignment purposes.

3.3.4.2 Vertical Beam Spot Position

VSAT_MONITOR vertical beam spot measurements were compared with the micro-vertex detector as described above.

The upper histogram of Figure 3.8 shows VSAT online vertical beam spot data *vs.* micro-vertex data for 74 runs from 11 LEP fills being rather close together in time (sample 1). That the **VSAT_MONITOR** vertical beam spot determination accuracy is lower than the horisontal one is seen in the figure, resulting in a worse fit to the micro-vertex ($\chi^2 = 3.312$). The reason is the superconducting quadrupole magnets in front of the VSAT modules, focusing outgoing particles in the vertical direction. The VSAT sensitivity to beam movements in this direction, which are often quite small, is therefore reduced accordingly.

Data from a later LEP fill was then added as shown in the lower histogram of Figure 3.8 (sample 2). The data from this fill can be seen clustered together in the lower left corner of the histogram. An approximately 1.1 mm vertical beam movement is visible, as measured by both **VSAT_MONITOR** and the micro-vertex, compared

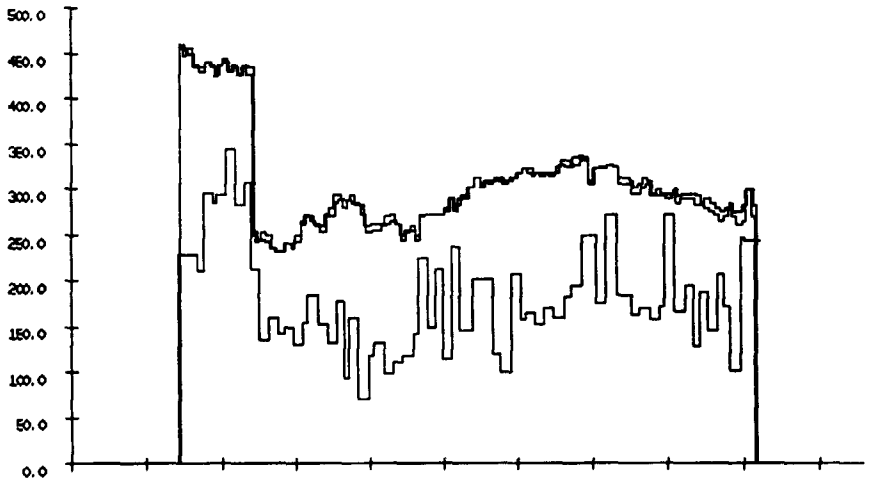

Figure 3.7: VSAT online and LEP BOM x-positions (μm). The two overlapping curves on top are BOM data for the electron and positron beams respectively.

to the compact cluster of sample 1. This quite large vertical beam movement in the 1991 LEP fills was also found by a full DELPHI beam spot analysis using micro-vertex, ID and TPC data [73]. The beam movement was due, at least partly, to LEP moving the quadrupole magnets in front of the VSAT [74]. This also explains why no scale factor was found between the VSAT and micro-vertex measurements.

From the above discussion, it is clear that the VSAT_MONITOR sensitivity to normal (*i.e.* small) vertical beam spot movements is low due to the quadrupole focusing effects. However, larger movements can be monitored.

3.3.4.3 Longitudinal Beam Spot Position

A run-by-run analysis of VSAT_MONITOR longitudinal beam spot estimates revealed the statistical errors to be too large for any conclusions to be drawn. Comparisons with the TPC were instead carried out on a fill-by-fill level, the results being shown in Figure 3.9. A linear relation between the two measurements is visible, the χ^2 being 1.495. Though the VSAT error bars are appreciable even when integrating over whole fills, useful longitudinal beam spot information is obtainable after only a few runs.

3.4 VSAT Monitoring of a Beam Separation Scan

In the spring of 1990 VSAT monitored a LEP beam separation scan. At this time VSAT was not included in the central DELPHI data aqcuisition, and the VSAT online monitoring routines were not fully developed. Data analysis was instead done offline. Full details of the beam separation scan is given in Appendix E.

From equation (3.1) it is seen that the accelerator luminosity is maximal when many beam particles collide in a small transverse area. The parameters of the beam

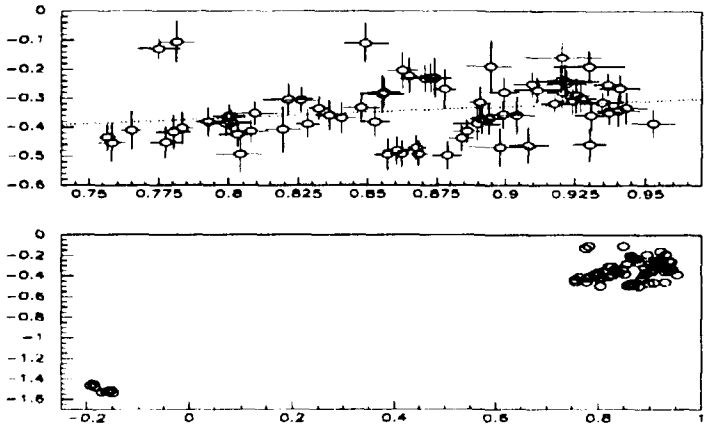

Figure 3.8: VSAT online *vs.* micro-vertex y-positions (mm) for sample 1 (upper histogram) and sample 2 (lower histogram).

optics should reflect this, they being tuned for maximal luminosity delivery. The beam separation scan was carried out in order to test the LEP beam optics.

The LEP beam bunches are highly elliptical, having nominal horisontal and vertical transverse dimensions of σ_x=300 μm and σ_y=12 μm respectively. The small vertical dimension leads to high demands on the vertical beam optics to ensure that the beams collide head-on. Optimal optics parameters were found by separating the beams in the vertical direction using electrostatic separators. Meanwhile VSAT measured the resulting Bhabha scattering event rates, these being proportional to luminosity according to (3.3).

Measurements were made at vertical beam separations of 0 μm, 10 μm, 20 μm and 30 μm. Both beams were moved symmetrically around the nominal zero position, and tests were performed with moving the electron-positron beams up-down as well as down-up. Two values of the LEP so-called β-function [75] were tried: β=7.0 cm and β=4.3 cm.

The nominal beam optics, *i.e.* 0 μm beam separation, was in all cases found to give maximum luminosity, confirming earlier LEP calculations. Changing the β-value from 7.0 cm to 4.3 cm lead to a measured luminosity increase of 22%.

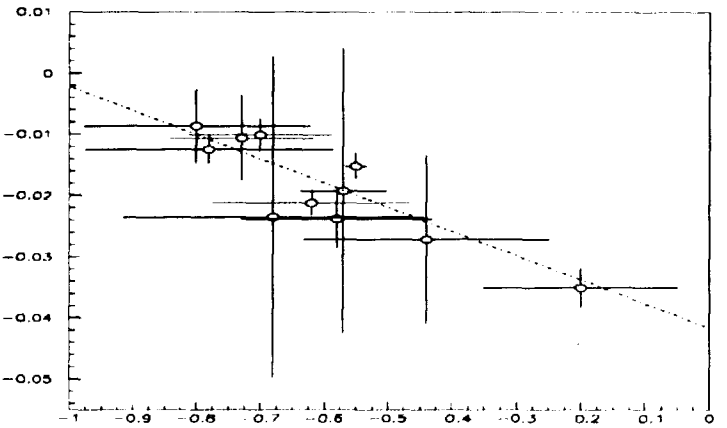

Figure 3.9: VSAT online *vs.* TPC z-positions.

Acknowledgements

I would like to thank my supervisor, Professor Göran Jarlskog, for patiently supporting me in every way and giving me the chance to do this work.

Being a Ph.D. student, many things are best learnt by working together with more senior physicists. I have been very fortunate to work with my collegues and friends Ulf Mjörnmark, Valery Pozdnyakov and Nikolai Zimin. I wish to thank them for their truly invaluable help.

Modern elementary particle physics experiments requires the co-operation of a large number of people, and a very large experiment like DELPHI is no exception. I would like to thank the members of the DELPHI Collaboration for providing a nice working environment and making this thesis possible. In particular, I thank Giuseppina Rinaudo of the VSAT group and Frederic Kapusta and Igor Tyapkin of the two-photon physics team for many fruitful discussions and much help.

Thanks are also due to everybody at the Department of Elementary Particle Physics in Lund. I have especially appreciated the good times and many laughs shared with my fellow-students Anders, Ivan, Lars and Olof.

The financial support from the University of Lund is gratefully acknowledged.

Bibliography

[1] J. Bjarne, Beam Monitoring in LEP, LUNFD6/(NFFL-7049)1988
[2] G.P. Ferri *et. al.*, CERN/ECP 90-8 CERN/SL 90-110 (BI)
[3] The LEP in short, Eds: M. Buhler-Broglin, D. Lajust, R. Lewis, CERN Publications, 1989
[4] Large Electron-Positron storage ring, Tecnical notebook, CERN Publications, 1989
[5] G. Guignard, LEP Parameter Note 9
[6] DELPHI Collaboration, Nucl. Instr. and Meth. A303(1991)233
[7] F. Hartjes *et. al.*, Nucl. Instr. and Meth. A256(1987)55
[8] C. Brand *et. al.*, Nucl. Instr. and Meth. A283(1989)567
[9] A. Amery *et. al.*, Nucl. Instr. and Meth. A283(1989)502
[10] P. Checchia *et. al.*, Nucl. Instr. and Meth. A248(1986)317
[11] G. Barichello *et. al.*, Nucl. Instr. and Meth. A254(1987)111
[12] P. Checchia *et. al.*, Nucl. Instr. and Meth. A275(1989)49
[13] L. Bugge *et. al.*, DELPHI 91-104 PHYS 147
[14] DELPHI Collaboration, CERN/LEPC/92-6, LEPC/P2-Add.1
[15] T. Camporesi *et. al.*, CERN-PPE/92-212
[16] PLUTO Collaboration, Ch. Berger *et al.*, Z. Phys. **C26**(1984)353
[17] TPC/2γ Collaboration, H. Aihara *et al.*, Phys. Rev. Lett. **58**(1987)97; TPC/2γ Collaboration, H. Aihara *et al.*, Phys. Rev. **D41**(1990)2667
[18] AMY Collaboration, R. Tanaka *et al.*, Phys. Lett. **B277**(1992)215
[19] ALEPH Collaboration, D. Buskulic *et al.*, Phys. Lett. **B313**(1993)509
[20] L3 Collaboration, O. Adriani *et. al.*, Phys. Lett. **318B**(1993)575
[21] OPAL Collaboration, R. Akers *et. al.*, Z.Phys. **C61**(1994)119
[22] F.M. Renard, Basics of Electron Positron Collisions, Editions Frontières, 1981
[23] H. Kolanoski, Two-Photon Physics at e^+e^- Storage Rings, Springer, 1984
[24] H. Kolanoski, P. Zerwas, High Energy Electron-Positron Physics, Eds: A. Ali, P. Söding, World Scientific, Singapore, 1988
[25] M. Feindt, CERN-PPE/91-90
[26] J.S. Steinman, Thesis, UCLA-HEP-88-004, 1988
[27] F. Naraghi, Thesis, Univ. Paris VII, 1992
[28] H.-U. Martyn, DESY 89-121 PITHA 89/20
[29] PLUTO Collaboration, Ch. Berger *et al.*, Phys. Lett. **B149**(1984)421
[30] TASSO Collaboration, M. Althoff *et al.*, Z. Phys. **C31**(1986)527
[31] CELLO Collaboration, H.J. Behrend *et al.*, Z. Phys. **C51**(1991)365
[32] J. Rosner, NBL Report 17522(1972)316
[33] J. Rosner, Brookhaven Report CRISP 7126 (1971)

[34] I.F. Ginzburg, V.G. Serbo, Phys. Lett. **B109**(1982)231
[35] J.J. Sakurai, D. Schildknecht, Phys. Lett. **B41**(1972)489
[36] B. Batyunya *et. al.*, DELPHI 94-76 PHYS 393
[37] B. Batyunya *et. al.*, DELPHI 93-60 PHYS 288
[38] J. Bjarne *et. al.*, DELPHI 93-90 PHYS 317
[39] R. Brun, D. Lienart, CERN Program Library Y250
[40] A.G. Frodesen, O. Skjeggestad, H. Tøfte,
Probability and Statistics in Particle Physics, Universitetsforlaget, 1979
[41] M. Drees, K. Grassie, Z. Phys. **C28**(1985)451
[42] H. Plothow-Besch, CERN/PPE 92-123
[43] DELPHI Collaboration, Z. Phys. **C62**(1994)357
[44] C. Bouvet, CERN SL/91-17 (BI)
[45] K. Potter, Proc. of the 1984 CERN Accelerator School, CERN 85-19
[46] H.J. Bhabha, Proc. Roy. Soc. **A.154**(1936)
[47] M. Caffo, E. Remiddi, Z Physics at LEP 1, Vol. 1, CERN 89-08
[48] M. Dam, L. Bugge, DELPHI 87-81 PHYS 21
[49] G. von Holtey, LEP Note 462
[50] H. Burkhardt *et. al.*, CERN SL/94-25 (EA)
[51] A.M. Smith, LEP Note 559
[52] P. Roudeau, LEP Note 472
[53] M.J. Clayton, G. von Holtey, P. Lienard, LEP Controls Note 94
[54] C. Gaspar, M. Dönszelmann DELPHI 94-4 DAS 148
[55] Yu. Belokopytov *et. al.*, DELPHI 93-2 PROG 193
[56] Ph. Charpentier *et. al.*, DELPHI 92-147 PHYS 240
[57] G. Jarlskog, M. Jonker, DELPHI 89-59 MIG 3
[58] J.A. Fuster *et. al.*, DELPHI 91-112 DAS 115
[59] M. Dönszelmann, C. Gaspar DELPHI 93-131 DAS 145
[60] Ph. Charpentier, C.M. Story, DELPHI 86-47 DAS 32
[61] Ph. Charpentier *et.al.*, Proc. of Computing in High Energy Physics '91
[62] M.J. Jonker *et.al.*, Proc. of Computing in High Energy Physics '91
[63] B. Franek *et.al.*, Proc. of IEEE 1991
[64] J. Bjarne, I. Kronkvist, U. Mjörnmark, VSAT Online Shift Instructions,
Internal VSAT report
[65] F. Bianchi, I. Kronkvist, DELPHI 92-116 PROG 190
[66] M. Koratzinos, VSAT Position Reconstruction, Internal VSAT report
[67] A. Håkansson, DELPHI 93-49 PHYS 279
[68] A. Håkansson, Thesis, Univ. of Lund, LUNFD6/(NFFL-7077)1993
[69] L. Lyons, DELPHI 91-97 PHYS 143
[70] DELPHI Collaboration, DELPHI 92-77 PHYS 188
[71] D. Johnson, D. Reid, W. Trischuk, DELPHI 92-36 PHYS 168
[72] G. Hamel de Monchenault, P. Jarry, Y. Sacquin, DELPHI 91-05 PROG 159
[73] P. Billoir, F. Ledroit, Tz. Spassoff, DELPHI 92-3 PHYS 152
[74] T. Taylor, Private communication
[75] H. Widemann, Particle Accelerator Physics, Vol. 1, Springer, 1993